筑　波　大　学

博 士 （ 医 学 ） 学 位 論 文

Construction of a single-cell atlas of non-hematopoietic cells in human lymph nodes and lymphoma for dissecting stromal remodeling

（ヒトリンパ節とリンパ腫における非血液細胞の一細胞アトラスの構築と間質リモデリングの解析）

2022

筑波大学大学院博士課程人間総合科学研究科

安部　佳亮

TABLE OF CONTENTS

LIST OF ABBREVIATIONS

ABEC	large artery
aBEC	arteriole
advSC	stromal cell at capsule adventitia
AGT-SC	AGT-positive stromal cell
aHEV	activated high endothelial venule
APC	allophycocyanin
$ATF3^{hi}$ SMC	smooth muscle cell with high ATF3 expression
$ATF3^{lo}$ SMC	smooth muscle cell with low ATF3 expression
BEC	blood endothelial cell
C7-SC	C7-positive stromal cell
caBEC	arteries surrounding the lymph node capsule
CAF	cancer-associated fibroblast
C-aHEV	transitional blood endothelial cell between capillary blood endothelial cell and activated high endothelial venule
cBEC	capillary blood endothelial cell
cLEC	ceiling lymphatic endothelial cell
collectLEC	collecting vessel lymphatic endothelial cell
CXCL10-HEV	CXCL10-positive high endothelial venule
DEG	differentially expressed gene
DLBCL	diffuse large B-cell lymphoma
Down-valve	lymphatic endothelial cell on the upstream side of valves
ECM	extracellular matrix
FDC	follicular dendritic cell
FITC	fluorescein isothiocyanate
FL	follicular lymphoma
fLEC	floor lymphatic endothelial cell
FSC	follicular stromal cell
GO	gene ontology
HEV	high endothelial venule
hHEV	homeostatic high endothelial venule

IF	immunofluorescence
IFR	interfollicular region
LEC	lymphatic endothelial cell
LN	lymph node
LNNHC	lymph node non-haematopoietic cell
MAST	model-based analysis of single-cell transcriptomics
MFLN	metastasis-free lymph node
mLN	mesenteric lymph node
MRC	marginal reticular cell
msLEC	medullary sinus lymphatic endothelial cell
NESC	non-endothelial stromal cell
NHC	non-haematopoietic cell
PC	pericyte
PCA	principal component analysis
PE	phycoerythrin
PE-Cy7	phycoerythrin-cyanin 7
PFA	paraformaldehyde
pfsLEC	perifollicular sinus lymphatic endothelial cell
pLN	peripheral lymph node
PvC	perivascular cell
PTCL	peripheral T-cell lymphoma
SC	stromal cell
scRNA-seq	single-cell RNA sequencing
SCS	subcapsular sinus
SFRP2-SC	SFRP2-positive stromal cell
SFRP4-SC	SFRP4-positive stromal cell
SMC	smooth muscle cell
tBEC	tip cell
tDLBCL	diffuse large B-cell lymphoma transformed from follicular lymphoma
TME	tumour microenvironment

TNF-SC	stromal cell enriched for tumour necrosis factor signalling
TRC	T-zone reticular cell
UMAP	Uniform Manifold Approximation and Projection
Up-valve	lymphatic endothelial cell on the upstream side of valves
VBEC	large vein

1. Background

1.1 Lymphoma

Lymphomas are the most common haematologic malignancies that often develop from lymph nodes (LNs). It is seventh and eighth common cancer in western countries and in Japan, respectively, and the incidence is higher in the elderly and increasing worldwide according to the population aging. Although some clinical factors have been suggested to increase the risk of lymphoma development, little is known regarding the causes of most lymphoma subtypes. Based on the recent classification[1], lymphoma is a highly heterogenous disease encompassing more than 80 subtypes with different pathological, genetical, and clinical features. Conventionally, they are categorized into Hodgkin and non-Hodgkin lymphoma and the latter is further roughly divided into B-cell and T/NK-cell lymphomas. Hodgkin lymphoma comprises approximately 5–15% of all lymphomas, whereas non-Hodgkin lymphoma comprises >80%. In non-Hodgkin lymphoma, B-cell lymphomas account for >80%. The representatives of B-cell lymphomas include diffuse large B-cell lymphoma (DLBCL) and follicular lymphoma (FL): the two subtypes account for more than half of non-Hodgkin lymphomas.

From a clinical point of view, common symptoms of lymphomas include painless lymphadenopathy, persistent fatigue, fever, night sweat, and unexplained wight loss,

although a part of patients experience disease site-specific symptoms such as neurological signs, shortness of breath, and abdominal distention. Lymphoma diagnosis is usually made pathologically on biopsy specimens of the swollen lymph nodes. Imaging tests including computerized tomography scan, blood tests, and cytogenetic examinations of the samples are also performed to support the diagnosis and/or to determine the clinical stage of lymphoma. Treatment depends on the subtype and stage of lymphoma and patient factors including age, comorbidities, and general status. Multidrug chemotherapy is selected in most of the lymphoma cases aiming at disease remission. Prognosis also varies by cases, lymphoma subtypes, and clinical stages. Recently, molecular targeted drugs such as anti-CD20 antibody are frequently used in many cases, which have greatly improved the clinical outcomes of lymphoma. Despite considerable advances in chemotherapies during the last decades, most lymphoma subtypes remain incurable; a significant part of patients finally experience relapse and disease-associated death. Therefore, new therapeutic approaches, including those targeting not only cancer cells but also the tumour microenvironment (TME), are needed[2,3]. In lymphomas, as in solid cancers[4,5], the activities of non-haematopoietic cells (NHCs), such as mesenchymal stromal cells (SCs) and endothelial cells, are thought to facilitate lymphomagenesis, and thus offer potential as therapeutic targets[2,3].

Indeed, some lymphoma subtypes reportedly exhibit unique interactions with NHCs[6-9], although lymphoma NHC research is far behind that of solid cancers[10].

1.2 Follicular lymphoma

FL is the second prevalent nodal non-Hodgkin lymphoma and the most common in indolent B-cell lymphomas. FL cells are considered to interact actively with NHCs to achieve emergence and expansion[9,11,12]. Notably, *BCL2/IGH* translocation, which has been considered a genetic hallmark of FL cells, is detected in blood cells of most healthy individuals at low levels, indicating that the translocation is insufficient for lymphoma development in itself and accumulation of secondary events are needed. Also, a waxing and waning disease course by spontaneous regression is relatively frequent in FL [1,13], emphasizing the supportive roles of TME. Indeed, specific mechanisms for supporting lymphomagenesis have been suggested in FL SCs. It has been found that SC-derived CXCL12 recruits FL cells in cooperation with CXCL13, which is produced by follicular dendritic cells (FDCs), contributing to follicular localization of tumor cells and their proliferation[9,14]. Other FDC-derived molecules, including BAFF, IL-15, and HGF, reportedly have anti-apoptotic effects on FL cells[15-17]. Unfortunately, a complete understanding of temporal and spatial associations underlying these activities is hampered by NHC heterogeneity. In fact, definitive NHC classification has not yet been achieved in humans, even in normal LNs[18,19]. Thus, the

identification of alterations in LN NHC (LNNHC) heterogeneity in the context of lymphomas is barely underway.

1.3 Non-hematopoietic cells in lymph nodes

LNs are characterized by the finely organized compartments that confers not only functional specificities but also optimal spatial relationships on LN niches. LNNHCs play crucial roles in maintaining LN compartments and in adapting LN structures for rapid and effective immune responses [20]. Major subsets of NHCs in LNs, as determined by morphology and topological localization, include blood endothelial cells (BECs) including high endothelial venules (HEVs), lymphatic endothelial cells (LECs), and non-endothelial SCs (NESCs)[19-21]. Examples of NESCs include T-zone reticular cells (TRCs), medullary reticular cells, perivascular cells (PvCs), and follicular SCs (FSCs), such as FDCs and marginal reticular cells (MRCs)[19-21]. Although recent investigations of NHC heterogeneity have employed emerging single-cell RNA sequencing (scRNA-seq) technology[22-27], which allows us to determine gene expression profiles of every single cells and uncover heterogeneities in the tissues, human LN BECs and NESCs have not been comprehensively analysed at single-cell resolution.

2. Research objectives

In this study, scRNA-seq was used to complete an atlas of human NHCs in LNs and lymphoma (Fig. 1). I aimed to identify previously unrecognized NHC heterogeneity in human LNs and dissect NHCs from lymphomas to define the global influences of lymphoma cells on the NHC niche. This approach can provide deep insights into lymphoma stromal biology and resources applicable to future studies on lymphomas, and also identify potential stroma-derived biomarkers that may serve as clinical indicators and/or therapeutic targets.

3. Materials and methods

3.1 Human samples

This study was approved by the Ethics Committee of the University of Tsukuba Hospital and the review boards of associated institutions that provided human samples (Kameda Medical Center, NTT Medical Center Tokyo, and Mito Medical Center) and conducted according to all relevant ethical regulations regarding human patients. Written informed consent was obtained from all participating patients. The participants were not compensated for their participation. For scRNA-seq, metastasis-free LN (MFLN) samples were prospectively collected from neoplasm-bearing patients (n = 9) who had undergone surgical LN dissection between January and June 2020. Non-sentinel LNs without enlargement (<1 cm) were used. The collected LNs were verified as malignancy-free via flow cytometric analysis of pan-cytokeratin negativity. Nodal FL (n = 10), peripheral T-cell lymphoma (PTCL) (n = 5), and DLBCL transformed from FL (tDLBCL) (n = 3) samples were also prospectively collected between August 2019 and May 2020. Furthermore, for functional experiments, additional nodal FL samples (n = 8) were collected between May 2020 and August 2021. Lymphoma diagnosis of tissue specimens was made pathologically, phenotypically, and/or referring to results of

cytogenetic examinations, including fluorescence *in situ* hybridization analysis by expert haematopathologists.

3.2 Single-cell isolation of LNNHCs

After collection, LN or lymphoma samples were immediately minced and digested for 1 h with RPMI 1640 medium (Sigma-Aldrich, R8758) with 5% fetal bovine serum containing 0.2 mg/ml collagenase P (Sigma-Aldrich, 11213857001), 0.8 mg/ml dispase (Gibco, 17105041), and 0.1 mg/ml DNase I (Worthington, LS002139), with continuous agitation. Cells were then filtered through a 70 μm mesh and red blood cells were lysed in 1% ammonium-chloride-potassium buffer. Thereafter, haematopoietic cells and contaminated red blood cells were depleted using human CD45 (130-045-801) and CD235a (130-050-501) microbeads according to the manufacturer's instructions (Miltenyi Biotec). For MFLN samples, the remaining single-cell suspension was incubated with phycoerythrin (PE)-anti-CD45 (Biolegend; 1:500) in combination with Alexa Fluor 488-pan-cytokeratin (ThermoFisher Scientific; 1:500), allophycocyanin (APC)-anti-podoplanin (Biolegend; 1:500), and PE-cyanin 7 (PE-Cy7)-anti-CD31 (Biolegend; 1:500). For lymphoma samples, PE-anti-CD45 was mixed with fluorescein isothiocyanate (FITC)-anti-CD31 (Biolegend; 1:500), APC-anti-podoplanin (Biolegend;

1:500), and PE-Cy7-anti-CD34 (Biolegend; 1:500). The samples were incubated for 20 min, then 7-AAD Viability Staining Solution (ThermoFisher Scientific, 00-6993-50; 1:1000) was added and incubated for 10 min in the dark on ice. CD45-negative live cells were sorted using FACSAria II or III (BD Bioscience) after removing doublets by gating with a FSC-H versus FCS-W plot and a SSC-H versus SSC-W plot. Flow cytometry data were analysed using FlowJo software (Tree Star Inc., v10.7.1). CD45-positive cells were cryopreserved in fetal bovine serum plus 10% dimethyl sulfoxide in liquid nitrogen.

3.3 Library preparation, sequencing, and data pre-processing

Sorted CD45-negative cells were converted to barcoded scRNA-seq libraries using Chromium Single Cell 3' Reagent kits (V3) (10X Genomics) according to manufacturer instructions (CG000183 Rev A), aiming for 5,000–8,000 cells per library. Library quality control and quantification were performed using a KAPA Library Quantification Kit for Illumina Platforms (Kapa Biosystems, KK4873) and a 2100 Bioanalyzer High Sensitivity DNA kit (Agilent, 5067-4626). Libraries were sequenced on an Illumina HiSeq X Ten system with an average depth of 31,439 reads per cell, then mapped to the

human genome (build GRCh38) and demultiplexed using CellRanger pipelines (10x Genomics, v3.1.0).

3.4 Data processing and cell clustering of individual cases

Pre-processed data from each sample were further processed and analysed individually using R package *Seurat* (v3.2.2) on RStudio (v3.5.0 or v4.0.2). After removing ribosomal genes, genes expressed in fewer than 3 cells, and cells expressing fewer than 200 genes, I filtered out cells with less than 200 unique feature counts (low quality cells). Cells with unique feature counts greater than three times the median value (possible doublets) and/or cells with more than twice the median number of mitochondrial genes (possible apoptotic or lysed cells) were also removed. I then normalized data using the "NormalizeData" function and extracted highly variable features using the "FindVariableFeatures" function. Normalized data underwent a linear transformation (scaling) and principal component analysis (PCA) based on variable features using the "RunPCA" function. Graph-based clustering was then performed according to gene expression profiles using the "FindNeighbors" and "FindClusters" functions with default parameters and results were visualized using a non-linear dimensional reduction Uniform Manifold Approximation and Projection (UMAP)

technique running “RunUMAP” and “DimPlot” functions. Cell clusters were annotated based on expression of canonical markers, including *PECAM1* and *JAM2* for BECs, *PECAM1* and *PROX1* for LECs, *ACTA2* for SMCs, *CCL19* and *CCL21* for TRCs, *CR2* for FDCs, *DCN* for other NESCs, *PTPRC* for contaminating lymphocytes, *SDC1* for plasma cells, and *CCR7* and *CD83* (in cells weakly *PTPRC*-positive) for dendritic cells[23,28,29]. *MKI67* and *TOP2A* expressions were used to identify clusters of an aggressively proliferative nature. In the FL sample 3, which came from a patient with intra-submandibular gland FL, any distinct clusters negative for all canonical markers and positive for keratin genes (indicating glandular tissue contamination) were removed. All other cases were confirmed to consist solely of these major clusters. I confirmed a negligible presence of ambient RNA contamination in single-cell NHC data, and found an imperceptible influence of potential RNA contamination on clustering results in all LN and lymphoma samples by using the *DecontX* (in the *celda* package, v1.6.1) and *SoupX* (v1.5.2) packages (data not shown)[30,31].

3.5 Data integration with batch effect collection

I performed canonical correlation analysis[32] to identify shared sources of variation across multiple datasets using the “FindIntegrationAnchors” function and integrated

them using anchors from the “IntegrateData” function with canonical correlation dimensions of 20. Integrated data were scaled and underwent PCA as performed in individual datasets.

3.6 Supervised annotation and unsupervised clustering of LNNHCs

I performed graph-based clustering of PCA-reduced integrated data and supervised annotation, as described in “Data processing and cell clustering of individual cases” above. Clusters characterized by extremely low unique feature counts (low quality cells) were removed.

Next, I extracted the three major NHC components (BECs, LECs, and NESCs) *in silico* and performed scaling, PCA-based dimensional reduction, and unsupervised graph-based sub-clustering of each component. I removed subclusters considered possible doublets as characterized by high expressions of marker genes for different NHC components and incongruously high unique feature counts. In BEC sub-clustering, I also performed supervised annotation for the identification of arterial, capillary, and venous BECs using canonical markers for each BEC component[33-36].

3.7 DEG analysis

DEG analysis was performed using the “FindMarkers” or “FindAllMarkers” functions with a minimum of 20% of the gene-expressing cells, and a minimum log fold-change of 0.25 in gene expression between each cluster and other clusters. I primarily used the Wilcoxon Rank-Sum test for DEG detection. To confirm detected DEGs, I also used model-based analysis of single-cell transcriptomics (MAST) method[37]. DEGs were defined as genes confirmed to show an adjusted *P* value (based on the Bonferroni correction) of <0.05 by using both methods. Results of the Wilcoxon Rank-Sum test were used to construct DEG lists and volcano plots. Volcano plots were created using the R package *EnhancedVolcano* (v1.8.0). DEG analysis to compare corresponding clusters between mLN and pLN samples and between MFLN and FL samples was performed in a similar manner using the cut-off parameters described above.

For DEG analyses between MFLN and FL NHC subclusters, I adopted a multistep approach. Several previous studies had indicated differences in gene and protein expression between mesenteric (mLNs) and peripheral (pLNs) LNs[38-41]. Therefore, I initially profiled DEGs between mLNs and pLNs among MFLNs at subcluster levels. Referring to this profile, I identified DEGs upregulated in FL by removing those detected between mLNs and pLNs. I also performed DEG analysis

between MFLN and FL NHC subclusters using only pLN samples (MFLN 7–9 and FL 2–10) to support reliability of detected DEGs.

Gene Ontology (GO) enrichment analysis of DEGs in particular clusters was performed using Metascape (http://metascape.org)[42].

3.8 Trajectory analysis

I performed trajectory analysis using the *Monocle 3* package (v0.2.3)[43] in RStudio on integrated BEC, NESC, and LEC data constructed by *Seurat*. Data pre-processing was performed using the "preprocess_cds" function with the number of dimensions set at 100. Dimensionality reduction and clustering were performed by the "reduce_dimension" and "cluster_cells" functions, respectively. I then fit a principal graph within each cluster using the "learn_graph" function and visualized the order of cells in pseudo-time by "plot_cells" or "plot_cells_3d" functions, as appropriate with the "pseudotime" colouring option.

3.9 Single-cell analysis of FL haematopoietic cells

I performed single-cell analysis of cryopreserved CD45-positive cells from nine FL samples (FL 2–10). After thawing, cell suspensions were filtered through a 70 μm mesh

and incubated with 7-AAD Viability Staining Solution for 10 min in the dark. The 7-AAD-negative live cells were sorted using FACSAria II or III after removing doublets, then were converted to barcoded scRNA-seq libraries, as performed in CD45-negative cells. Library preparation, sequencing, and data processing were performed as for CD45-negative cells. Data quality control, processing, and graph-based clustering were performed in each individual case using the *Seurat* package with dimension and resolution parameters of 50 and 0.5, respectively. Thereafter, I identified malignant B-cell populations by detecting restrictions of light chain kappa/lambda genes, as suggested by previous studies[44,45]. Briefly, I projected B-cell marker *CD79A* and light chain genes *IGKC* (for light chain kappa) and *IGLC2* (for light chain lambda) to cell clusters on the UMAP plot of each sample. I then calculated the ratio of cells expressing *IGLC2* and *IGKC* with expression levels of >1 and >2, respectively, in each B-cell cluster. I defined B-cell clusters with a ratio of >2.0 or <0.25 as malignant.

3.10 Malignant B-cell signature analysis in FL B cells

To support the reliability of malignant B-cell detection, I performed signature analysis on data from FL B cells. I developed a gene set that represents a malignant B-cell signature based on the recent single-cell analysis of FL B cells reported by Andor et

al[44]. I carefully selected genes that were described as significantly upregulated in malignant compared to non-malignant B cells in a uniform manner among different FL samples[44]. A malignant B-cell signature score was calculated in B cells of all nine FL samples using the *GSVA* package (v1.38.2)[46] and depicted by the "FeaturePlot" and "VlnPlot" functions of *Seurat*.

3.11 Intercellular ligand–receptor interaction analysis

I investigated interactions between NHC subclusters and malignant B cells of nine FL samples (FL 2–10) using the *CellPhoneDB* package (v2.1.1)[47] on Python (v3.6). Gene expression information relevant to each NHC subcluster in integrated FL NHCs was used for NHC data, while gene expression information relevant to malignant B-cell clusters in each FL sample was separately used for malignant B-cell data, since gene expression profiles of malignant B cells vary greatly among samples. I then performed pairwise comparisons between NHC subclusters and malignant B-cell clusters. Briefly, I derived potential ligand–receptor interactions based on expression of a receptor gene by one lineage subpopulation and a ligand gene by another. I filtered genes expressed in >20% of cells in any given subpopulation. I then permuted the cluster labels of all input cells 1,000 times and calculated the mean interaction score (the average receptor

expression level in a subpopulation multiplied by the average ligand expression level in the interacting subpopulation), generating a null distribution of the mean interaction score for each ligand–receptor pair in each pairwise comparison across subpopulations. Thereafter, I located observed mean interaction scores that were the same or higher than the actual mean score in the null distribution and calculated the proportion of the observed scores, conferring a *P* value for the likelihood of specificity of a given ligand–receptor complex to a given cluster pair. To consider interactions between FL NHCs and FL malignant B cells, I selected only interactions with a *P* value of <0.05 in more than half of FL cases (>4 cases). Furthermore, to assess subcluster-specific lymphomagenesis mechanisms in FL stroma, I extracted interactions that included a molecule in which gene expression was significantly upregulated in at least one FL NHC subcluster compared with that in the corresponding MFLN subcluster. I integrated interaction scores and *P* values of interactions between pairs consisting of the same NHC subcluster and malignant B-cell clusters from different FL samples, as previously described[45]. Briefly, I calculated mean interaction scores for pairs that included the same NHC subcluster and malignant B-cell clusters from different FL samples, then normalized the mean interaction scores per interaction. I also combined *P* values of interactions for pairs that consisted of the same NHC subcluster and malignant B-cell

clusters from different FL samples using Fisher's method. The *P* values were corrected using the Benjamini–Hochberg method.

3.12 Immunofluorescence staining

Human LN and lymphoma samples were immediately embedded in OCT compound (Sakura Finetek Japan Co., 45833) and frozen in hexane cooled with dry ice. Samples were sliced to 3-μm thickness with a cryostat at -20 ℃. Sections were dried for 1 h at 20 ℃, fixed for 10 min in 4% paraformaldehyde (PFA), incubated for 10 min with 0.1% Triton X-100 (Sigma-Aldrich, T9284) for permeabilization, and then treated with 10% goat serum (Sigma-Aldrich, G9023) in PBS or serum-free protein blocking buffer (Dako, X0909) (when using non-goat-derived secondary antibodies) for 30 min of blocking. Sections were stained overnight at 4 ℃ with primary antibodies. After several TBS-T washes, sections were stained for 1 h with the combinations of the following secondary antibodies at 20 ℃: AF488-goat-anti-rat IgG (ThermoFisher Scientific), AF594-goat-anti-rabbit IgG (ThermoFisher Scientific), AF594-donkey-anti-goat IgG (ThermoFisher Scientific), and AF647-goat-anti-mouse IgG (ThermoFisher Scientific). The TrueVIEW Autofluorescence Quenching Kit (VECTOR, SP-8500) was used to decrease possible tissue autofluorescence, following manufacturer instructions. Sections

were then mounted in Mounting Medium with DAPI (VECTOR, H-1200). Stained samples were imaged using a Leica DMi8 S Platform with the THUNDER imaging system (3D Live Cell & 3D Cell Culture & 3D Assay). Analysed LNs were verified as malignancy-free by pan-cytokeratin staining. Quantitative analysis of acquired images was performed using ImageJ software (National Institute of Health, v2.1.0). Since LNs and FL carry localized structures, I randomly acquired at least five different regions of interest within each sample and used the median values for statistical analysis.

3.13 Flow cytometric analysis of FL haematopoietic cells

To analyse the expression of CD27 in malignant FL B cells and to perform binding/adhesion assays described below, I used additionally collected cryopreserved FL samples (FL 11–18). After thawing, cells were filtered through a 70 μm mesh, and incubated with PE-anti-CD27 (Biolegend; 1:500), FITC-anti-CD3 (Biolegend; 1:500), APC-anti-CD19 (Miltenyi Biotec; 1:500), and PE-Cy7-anti-CD10 (Biolegend; 1:500) antibodies for 20 min on ice. Cells were then incubated with 7-AAD Viability Staining Solution for 10 min in the dark and analysed using FACSAria II or III and FlowJo software.

3.14 Recombinant protein binding assay

Recombinant Fc chimera CD70 (SinoBiological, 10780-H01H) or human IgG (R&D systems, 1-001-A) was incubated with a single-cell suspension of FL haematopoietic cells for 10 min at 4 ºC in RPMI with 10% FCS. To block CD70–CD27 binding, cells were incubated in the presence of anti-CD27 blocking antibody (R&D systems, MAB382) or isotype mouse IgG1 (R&D systems, MAB002) for 30 min at 4 ℃ before binding. After binding, the cells were washed, fixed by 4% PFA for 10 min at 20 ℃, incubated with PE-anti-human IgG Fc (R&D systems; 1:500), FITC-anti-CD3 (1:500), APC-anti-CD19 (1:500), and PE-Cy7-anti-CD10 (1:500) for 20 min at 4 ºC, and analysed using flow cytometry (FACSAria II or III) and FlowJo software.

3.15 *Ex vivo* cell adhesion assay

Frozen FL sections were sliced at 6-μm thickness immediately before the assay. For malignant B-cell isolation, I used FL samples in which >90% B cells were confirmed to be malignant by using flow cytometric analysis. B cells were isolated from the FL haematopoietic cell suspension using the EasySep Release Human CD19 Positive Selection Kit (STEMCELL Technologies, ST-17754). Cells were then treated with anti-CD27 blocking antibody or isotype mouse IgG1 for 30 min at 4 ℃. Thereafter, 2×10^6

cells were applied on the sections and incubated with a 60-rpm rotation for 5 min, followed by incubation without rotation for 15 min. The incubation with and without rotation was repeated two more times. After incubation, the sections were gently washed with PBS, sealed with a cover glass, and imaged using a Keyence BZ-X710 microscope (Keyence). Adherent cells were manually counted with ImageJ.

3.16 Prognostic analysis of stroma-derived markers in FL

To analyse prognostic potential of gene expression patterns of NHCs in FL patients, I used a bulk microarray dataset of 180 biopsied FL samples from independent, newly diagnosed cases[48]. To narrow candidates to stroma-specific genes, I initially selected DEGs upregulated in FL BEC and NESC subclusters relative to MFLN counterparts. These were narrowed down to those showing a log fold-change of >0.5 and a <0.1% of cells with an expression level higher than 0 in FL haematopoietic cells. I did not use genes upregulated in FL LEC subclusters, as the proportion of FL LECs was considerably decreased relative to MFLN LECs and the specificity of these genes to FL stroma was considered unlikely in analyses of bulk tissues. Next, I tested expression of all candidate genes by using the Kaplan–Meier method using a two-sided log-rank test. Cutoff expression values of each gene for the Kaplan–Meier survival curves was

determined using maximally selected rank statistics[49]. Since many putative stroma-specific genes were upregulated in FL, it was possible that *P* value collection (e.g. the Bonferroni method) greatly reduced the number of candidate genes, considering that the sample size in the dataset was not particularly large. Therefore, I extracted genes with reliable prognostic impacts using another approach. I initially divided patients into three groups according to survival outcomes: a favourable group, including patients alive 10 years post-diagnosis; an unfavourable group, including patients who died within 5 years of diagnosis; and an intermediate/indefinite group, including the remaining patients. I then compared the proportion of patients with higher expression of each candidate gene between favourable and unfavourable groups. Genes were considered prognostic when the proportion was significantly higher in the unfavourable group compared to that in the favourable group. These prognostic genes were further subjected to multivariate analysis.

To evaluate the prognostic efficiency of FL TRC signature, I extracted the DEGs which were upregulated in FL TRCs in comparison to MFLN TRCs. I considered the DEGs with an expression level higher than 0 in <0.1% FL haematopoietic cells, <10% FL BECs, and <10% FL LECs and were detectable in the microarray dataset[48].

3.17 Whole-exome sequencing

Whole-exome sequencing was performed on genomic DNA extracted from nine FL samples (FL 2–10). Libraries were prepared using SureSelect Human All Exon v7 kits (Agilent Technologies, 5191-4004) according to the manufacturer's instructions and sequenced using an Illumina HiSeq X Ten system with a 150-bp paired-end protocol. I used the *Genomon2* pipeline (v2.6.2) for alignment of sequence and mutation calling. Somatic mutations with a Fisher's exact *P* value of <0.01 and an empirical Bayesian call *P* value of <0.0001 were adopted. Thereafter, mutations of synonymous single nucleotide variants; variants only in unidirectional reads; variants in intergenic, intronic, untranslated regions, and noncoding RNA regions; and variants in repetitive genomic regions were excluded. Furthermore, known genetic alterations affecting at least 10% of FL[11] were screened for additional mutations. Finally, mutations derived from mapping errors were excluded using the Integrative Genomics Viewer.

3.18 Statistics and reproducibility

Statistical analysis was performed using R on RStudio or GraphPad Prism 9 (GraphPad, v9.2.0). A two-sided *P* value of <0.05 was considered statistically significant.

4. Results

4.1 Transcriptional features of major NHC components

To profile NHCs in human LNs and lymphomas, I performed scRNA-seq and data integration of NHCs extracted from LN samples without tumour-cell infiltration (MFLNs) from nine neoplasm-bearing patients, and nodal FL samples from ten patients (Table 2). Graph-based clustering of integrated cells led to the identification of three major NHC components (BECs, LECs, and NESCs) and three contaminating haematopoietic cell components (lymphocytes, plasma cells, and dendritic cells) on the UMAP (Fig. 2a). Cell type annotation was performed based on expression analysis of canonical gene markers (Fig. 2b) and differentially expressed gene (DEG) analysis (Fig. 2c). Clustered NHCs were uniformly distributed across patients, cohorts, sample collection sites, and patient ages (Fig. 2a,d,e). Notably, expression of the marker *PDPN*, which has been used for LEC isolation in recent scRNA-seq studies[23-25], was either partially decreased or absent in LECs (Fig. 2f). Accordingly, the proportion of LECs among NHCs detected using flow cytometric analysis was slightly smaller than that determined using scRNA-seq, although I observed excellent concordance in the proportion of each NHC component between both methods (Fig. 2g).

To identify subclusters within each of these three major NHC components, I extracted each NHC component *in silico* and subjected it to re-clustering. Surprisingly, NHCs of MFLN and FL were similarly distributed (Fig. 2h), in contrast with observations in solid cancers[50,51]. Here, I first sought to construct a single-cell atlas of NHCs in MFLNs.

4.2 Human LN BECs: ten subclusters

I identified arterial, capillary, and venous BECs (Fig. 3a). Venous BECs were most prevalent in MFLNs, followed by capillary and arterial BECs (Fig. 3b). For this annotation, I used known markers, including *GJA4* for arterial, *CA4* for capillary, and *ACKR1* for venous BECs (Fig. 3c,d)[33-35].

Unsupervised clustering in BECs further revealed 10 transcriptionally distinct subclusters: large arteries (ABECs), arteries surrounding the LN capsule (caBECs), arterioles (aBECs), tip cells (tBECs), capillary BECs (cBECs), transitional BECs between capillary BECs and activated HEVs (C-aHEVs), activated HEVs (aHEVs), homeostatic HEVs (hHEVs), CXCL10-positive HEVs (CXCL10-HEVs), and large veins (VBECs) (Fig. 3e,f). Each exhibited over 100 DEGs that helped in clearly distinguishing the groups (Fig. 3g–k).

ABECs, aBECs, tBECs, cBECs, and VBECs had reasonable counterparts with similar gene expression profiles in mouse tissues including LNs[26,36] or in other human tissues[51]. ABECs are characterized by selective expression of *GJA5* (Fig. 3h–j), defined as a marker of larger arteries in murine tissues, including LNs[26,36]. By contrast, caBECs specifically express *SSUH2* (Fig. 3h–j), a marker of arteries of varying size in different mouse tissues[36]. aBECs are characterized by expression of *INSR* (Fig. 3j) and *EDNRB*

(Fig. 3i), both capillary markers in mouse livers, lungs, and colon[36]. tBECs belong to a small but highly distinct subcluster that selectively expresses *PGF* and *LY6H* (Fig. 3h–j). *PGF* is described as an endothelial tip cell marker in human lung cancer[51], whereas *LY6H* has not been shown to be a specific marker in mice or humans[36]. Other human tip cell markers, including *CXCL4*[51], were identified as DEGs in tBECs (Fig. 3h). cBECs are characterized by abundant *PLVAP* and *CA4* expression (Fig. 3h–j), in agreement with mouse data describing them both as capillary markers in multiple tissues[36]. C-aHEVs express DEGs of cBECs (including *CA4*) and aHEVs (Fig. 3h–j), indicative of the transitioning nature of C-aHEVs. Also, *HES1*, a capillary marker in several mouse tissues, was highly expressed in C-aHEVs (Fig. 3h)[36]. C-aHEVs and aHEVs express genes encoding heat shock proteins (*HSPA1A*, *HSP90AA1*, and *HSPA1B*), as well as those involved in NFkB (*NFKBIA* and *NFKBIZ*) and JNK (*JUN*, *JUNB*, *JUND*, *FOS*, and *FOSB*) activation. They also express genes associated with oscillatory shear stress (*EGR1*, *ICAM1*, *MT2A*, *MT2X*, and *ADM*) at higher levels than do cBECs and hHEVs (Fig. 3k)[52]. aHEVs, hHEVs, and CXCL10-HEVs all express genes specific to HEVs, including *ACKR1*, *C7*, and *CH25H*[41] (data not shown). aHEVs were characterized by prominent expression of *G0S2* (Fig. 3h), which is upregulated following induction of cell-cycle progression[53], and *SELE* (Fig. 3h–j), which is upregulated by inflammation[54].

In contrast, hHEVs expressed *SELE* at low levels (Fig. 3i). CXCL10-HEVs are unique in their expression of the chemokines *CXCL9*, *CXCL10*, and *CXCL11* (Fig. 3h–j). VBECs are characterized by high expression of *CPE* and *VCAM1* (Fig. 3h), which are markers of large veins[26,36].

I next performed trajectory analysis on integrated MFLN BEC data using the *Monocle 3* pipeline[43]. I was able to identify all BEC subclusters in a *Monocle 3*-generated cell object (Fig. 3l). Trajectory of the arterial component flowed from ABECs to aBECs and cBECs, finally reaching tBECs (Fig. 3m). Similarly, trajectory of the venous component initially traced HEV subclusters (aHEVs and hHEVs), then proceeded to capillary subclusters (C-aHEVs and cBECs) and finally to tBECs (Fig. 3m). These findings support the idea that tBEC migration in LNs generates new capillary BECs[55].

Gene ontology (GO) analysis revealed that factors involved in blood vessel development were enriched in ABECs, caBECs, aBECs, and tBECs (Fig. 3n), in agreement with their arterial or tip cell nature. Leukocyte migration and cellular extravasation signatures were most enriched in aHEVs (Fig. 3n). Molecules associated with apoptosis were enriched in C-aHEVs and aHEVs (Fig. 3n). Also, as reported in

mice[26], CXCL10-HEVs expressed molecules associated with interferon and cytokine signalling (Fig. 3n).

Immunofluorescence (IF) staining identified GJA5-, SSUH2-, and INSR-positive BECs as large arterial BECs in LNs (ABECs), arterial BECs outside of LNs (caBECs), and arterioles (aBECs), respectively (Fig. 3o–q). I also detected tBECs as LY6H- or PGF-positive cells in the tips of PLVAP-positive capillary BECs (cBECs) (Fig. 3r,s). Staining for PLVAP, HES1, and the HEV marker MECA-79 revealed that $PLVAP^{+}HES1^{+}$ capillary BECs (C-aHEVs) and $MECA\text{-}79^{+}HES1^{+}$ HEVs (aHEVs) (Fig. 3k) were localized near each other (Fig. 3t). HEVs strongly expressing SELE (aHEVs) were frequently observed in interfollicular regions (IFRs) (Fig. 3u), indicating that IFRs may serve as niches that play pivotal roles in promoting influx of immune cells into LNs. Notably, CXCL10-HEVs were frequently observed in IFRs and localized exclusively in the vicinity of aHEVs (Fig. 3v). These findings, together with GO analysis, suggest that rare CXCL10-HEVs may activate cellular trafficking of adjacent HEVs via cytokine signalling, resulting in the heterogeneity of human HEVs.

I examined the expression of marker genes for mouse LN BEC subclusters[26] in our human BEC data and summarized an assumed correspondence relationship between mouse and human LN (Fig. 3w,x).

In short, our single-cell atlas of LN BECs identified three, three, and four transcriptionally distinct subclusters in arterial, capillary, and venous BECs, respectively, showing unique heterogeneity in humans (Fig. 3y).

4.3 Human LN LECs: eight subclusters

A human LEC atlas recently proposed the following six LEC subclusters: subcapsular sinus (SCS) ceiling LECs (cLECs; LEC I), SCS floor LECs (fLECs; LEC II), particular SCS ceiling LECs that cover medullary regions (LEC III), capillary LECs in surrounding tissues (LEC IV), valve LECs (LEC V), and LECs of medullary and cortical sinuses (LEC VI)[23,24].

Accordingly, I performed unsupervised clustering of MFLN LECs, DEG and trajectory analyses, and IF staining to compare results across studies. Putative cLECs (LEC I), particular SCS ceiling LECs that cover medullary regions (III), capillary LECs in surrounding tissues (IV), and valve LECs (V) were observed in our clustering, as suggested by Takeda et al and Xiang et al[23,24], though I annotated LECs III and IV as collecting vessel LECs (collectLECs) and medullary sinus LECs (msLECs), respectively (Fig. 4a,b).

DEG analysis has revealed that the "fLEC and perifollicular sinus LEC (pfsLEC)" subcluster is unique in harbouring more than twice as many DEGs as other LEC subclusters (Fig. 4c–f). These DEGs include chemokine genes such as *CXCL1*, *CXCL5*, and *CCL20* (Fig. 4c,d,f), and genes associated with immune cell adhesion, including *ICAM1*, *VCAM1*, and *SELE*, supporting the immunological function of fLECs

in cell trafficking and migration. Genes reportedly specific to pfsLECs (e.g. *MARCO* and *CLEC4G*[24]) were also detected as top DEGs for the "fLEC and pfsLEC" subcluster (Fig. 4d,f)[23,24]. *ACKR4*, *MFAP4*, *CCL21*, *CLDN11*, and *GJA4* were also consistently identified as top DEGs for cLECs, collectLECs, msLEC, valve LECs (both Up- and Down-valves), and down-valves, respectively (Fig. 4c,d,f)[23].

To verify that a single "fLEC and pfsLEC" subcluster consists of both fLECs and pfsLECs, I applied unbiased sub-clustering analysis to the "fLEC and pfsLEC" subcluster. As expected, it comprised two transcriptionally distinct populations (Fig. 4g). In agreement with the findings of Takeda et al, the proportion of pfsLECs was smaller than that of fLECs (Fig. 4h)[23]. Notably, in DEG analysis between fLECs and pfsLECs, genes described as specific to LEC II and VI[23] were separately detected as top DEGs for fLECs and pfsLECs, respectively (Fig. 4i).

Next, I performed trajectory analysis on integrated LEC data. I identified all LEC subclusters in a *Monocle 3*-generated cell object (Fig. 4j). As expected, bLECs and collectLECs were adjacent to cLECs (Fig. 4k). Remarkably, a trajectory from fLEC and pfsLEC subclusters connected with remaining LEC subclusters in the middle region of bLECs and msLECs, and a direct trajectory connection was observed between pfsLECs and msLECs (Fig. 4k), supporting positional relationships inferred across these

subclusters[24]. Both Up- and Down-valves were connected to collectLECs (Fig. 4k), supporting the annotation of collectLECs.

IF staining showed that PAI1- (encoded by *SERPINE1*) positive bLECs were exclusively embedded in the intermediate area of the SCS (Fig. 4l). PTX3-positive LECs (msLECs) were preferentially located at the medulla (Fig. 4m), although a small proportion of cLECs also showed PTX3 positivity (Fig. 4c). MARCO-positive LECs (pfsLECs) were preferentially situated at perifollicular sinuses (Fig. 4n), as shown in mice[24]. MFAP4-positive LECs (collectLECs) were observed only in afferent and efferent collecting vessels (Fig. 4o).

Our analysis thus identified a total of eight LEC subclusters unifying data from recent reports (Fig. 4p,q)[23-25].

4.4 Human LN NESCs: twelve subclusters

NESCs were divided into 12 subclusters: SCs at capsule adventitia (advSCs), SFRP4-positive SCs (SFRP4-SCs), SFRP2-positive SCs (SFRP2-SCs), SCs enriched for tumour necrosis factor (TNF)-signalling (TNF-SCs), C7-positive SCs (C7-SCs), AGT-positive SCs (AGT-SCs), TRCs, pericytes (PCs), smooth muscle cells (SMCs) with high or low ATF3 expression ($ATF3^{hi}$ or $ATF3^{lo}$ SMCs), MRCs, and FDCs (Fig. 5a,b). TRCs, PCs, MRCs, and FDCs were annotated based on conventional taxonomy[19].

DEG analysis revealed that NESC subclusters exhibited over 100 DEGs each (Fig. 5c). advSCs showed the highest *CD34* expression among NESCs (Fig. 5d) and are considered the human counterpart of mouse $CD34^{+}$ SCs observed at adventitia of the LN capsule[22]. Both SFRP4-SCs and SFRP2-SCs shared *SFRP2* expression, and were discriminated by higher *SFRP4* expression in the former (Fig. 5d,e). SFRP4-SCs also showed relatively high *INMT* expression (data not shown), suggesting they are the counterpart of mouse $Inmt^{+}$ SCs observed exclusively at medullary cords[22]. TNF-SCs were specifically characterized by *PTX3* expression, and C7-SCs by abundant *C7* expression (Fig. 5d,e). AGT-SCs expressed *AGT* and high levels of the apolipoprotein genes *APOE* and *APOC1* (Fig. 5d,e). TRCs were marked by high *CCL19* and *CCL21* expression (Fig. 5d,e)[19], and PCs by specific expression of *NDUFA4L2* and *HIGD1B*

(Fig. 5d,e)[56]. ATF3^{hi} and ATF3^{lo} SMCs both expressed muscle-specific *MYH11* and *PLN* (Fig. 5d,e) but differed in expression of genes associated with cellular responses to stress or mechanical stimuli (Fig. 5f). Approximately half of MRC DEGs were seen in FDC DEGs (data not shown), consistent with the idea that MRCs differentiate into FDCs[21]. FDC markers *FDCSP*, *CR2*, and *FCER2* were correctly detected as FDC-specific DEGs (Fig. 5d,e). Intriguingly, *TNFSF13B*, which encodes B cell-activating factor belonging to the TNF family (BAFF) and is thought to define FDCs[21], was expressed by both MRCs and FDCs, but more highly by MRCs (Fig. 5d,e).

All NESC subclusters were identified in *Monocle 3*-generated cell objects (Fig. 5g,h). Trajectory analysis revealed that MRCs were connected to TNF-SCs and C7-SCs (Fig. 5i), indicating that the latter two subclusters might possibly differentiate into MRCs. Additional analysis showed a continuous trajectory from SMC subclusters to PCs, TRCs, MRCs, and finally to FDCs in human LNs (Fig. 5j), consistent with findings in mice of fibroblastic reticular cells in the splenic white pulp[57].

GO analysis revealed high expression in advSCs of genes functioning in formation of elastic fibres and extracellular matrix (ECM) (Fig. 5k)[58]. In agreement with the preferential localization of mouse Inmt^{+} SCs at the medulla[22], their human counterparts, SFRP4-SCs, abundantly expressed genes involved in ECM formation

(Fig. 5k). TNF-SCs expressed genes associated with TNF signalling (*IL6* and *CCL2*) (Fig. 5k), suggesting that they function in chemotaxis of CCR2-expressing T cells, monocytes, and dendritic cells to antigen sites[59]. C7-SCs expressed genes related to chemotaxis regulation (Fig. 5k), including *CXCL12* (Fig. 5d), which supports transendothelial T-cell migration across HEVs[60]. Top DEGs for AGT-SCs included *APOE*, *AGT*, and *LPL*, which participate in remodelling of protein-lipid complexes and plasma lipoprotein particles (Fig. 5k), suggesting that AGT-SCs may participate in lipid metabolism or transport. TRCs were enriched with GOs related to leukocyte and dendritic cell migration (Fig. 5k), in accordance with their reported function in recruiting naive T cells and dendritic cells to the T-cell zone to facilitate interaction[19]. Genes associated with smooth muscle structure or contraction were enriched in PCs and in SMC subclusters, whereas PCs abundantly expressed genes associated with blood vessel development (Fig. 5k). MRCs and FDCs were highly enriched with GOs relevant to cytokine- and chemokine-mediated signalling and antigen processing and presentation (Fig. 5k), consistent with their role in positioning and presenting antigens to B cells[19]. Finally, FDCs expressed genes involved in immunoglobulin-mediated immune response and B-cell-mediated immunity (Fig. 5k)[19].

IF staining was performed to identify the localization of each subcluster in the LNs (Fig. 5l–w). Fibroblasts positive for decorin (encoded as *DCN*), a strong marker of advSCs, SFRP4-SCs, SFRP2-SCs, TNF-SCs, and C7-SCs (Fig. 5l), were distributed widely in the adventitia, IFRs, and medulla (Fig. 5m). FBN1-positive SCs (advSCs) (Fig. 5d) were observed at the capsule adventitia, as observed in mice (Fig. 5n)[22]. SFRP2-positive SCs (SFRP2-SCs and SFRP4-SCs) were preferentially distributed in the medulla (Fig. 5o). PTX3-positive SCs (TNF-SCs) were observed in IFRs (Fig. 5p). C7-SCs were most frequent in the outer cortex, excluding follicles (Fig. 5q), consistent with their proposed role in facilitating immune cell migration. AGT-positive cells were found on outer regions of the IFRs, frequently situated between SCSs and HEVs (Fig. 5r). SMCs were observed as α-smooth muscle actin (encoded by *ACTA2*)-, MYH11-, or PLN-positive cells (Fig. 5d) around not only arterial BECs, but some HEVs as well (Fig. 5s). ATF3 was positive in some SMCs around HEVs in the IFRs (aHEVs), as well as around arteries (Fig. 5t). In line with DEG analysis between SMC subclusters, ATF3-positive SMCs were also marked by HSP70 (encoded by *HSPA1A*) expression (Fig. 5u), probably reflecting cell damage induced by blood flow[61] and/or immune cell trafficking. HIGD1B-positive cells (PCs) were observed around BECs, including arteries and HEVs (Fig. 5v), and were more prevalent around HEVs in IFRs (aHEVs) than around hHEVs

(Fig. 5v), indicating that they may support lymphocyte recruitment and maintain endothelial cell integrity[19]. MRCs and FDCs were identified as BAFF- and CR2 (also known as CD21)-positive, respectively (Fig. 5w).

I examined the expression of key genes for mouse LN NESC subclusters[22] in our human NESC data and assumed a correspondence relationship between mouse and human LNs (Fig. 5x,y).

To summarize, I identified 12 NESC subclusters, showing unanticipated heterogeneity, linked to the distribution of other NHC subsets and LN niches (Fig. 5z).

I thus accomplished a single-cell atlas of NHC components in human LNs (Fig. 5z).

4.5 Additional basic information of the single-cell LNNHC atlas

All subclusters identified in the single-cell LNNHC atlas included cells from all MFLN samples with some variations in cell proportion (Fig. 6a). Notably, NHCs from a patient with a benign tumour (MFLN 8) were distributed uniformly among NHCs from all MFLN samples (Fig. 6b). Furthermore, in NHC subclusters harbouring at least 50 cells from the sample MFLN 8, 80–100% of the top DEGs for all MFLN sample subclusters matched MFLN 8 DEGs (Fig. 6c).

I also profiled DEGs between mLN and pLN NHC subclusters using MFLN data (Fig. 7a,b). In this dataset, I observed markedly higher expression of *MADCAM1* in mLN HEV subclusters (aHEVs and hHEVs) compared with pLN counterparts (Fig. 7a). Consistently, GO analysis of DEGs between mLN and pLN subclusters showed that mLN HEV subclusters were enriched with *MADCAM1*-containing GO terms associated with cell adhesion and interactions with integrin (Fig. 7b). I also found that multiple mLN NHC subclusters (particularly, NESC subclusters) highly expressed genes associated with inflammatory response including *PTX3*, *CCL2*, and *TNFAIP6* relative to pLN counterparts (Fig. 7a,b). GO terms associated with inflammatory response, TNF-signalling, and response to molecules of bacterial origin were enriched in mLN LEC and NESC subclusters (Fig. 7b). Additionally, pLN LEC and NESC subclusters

abundantly expressed genes associated with the maintenance of LN homeostasis and structures (Fig. 7a,b).

4.6 Remodelling of non-haematopoietic cell proportions in FL

Using this atlas, I next sought to explore alterations in FL NHCs at subcluster levels by comparing with MFLN counterparts (Fig. 8a,b). Overall, the proportion of BECs markedly increased in FL relative to MFLNs, while the proportion of LECs decreased (Fig. 8b). Moreover, the proportion of arterial subclusters increased in FL BECs (Fig. 8b). In FL NESCs, the proportion of FDCs greatly increased (Fig. 8b). Notably, MRCs also dramatically increased in FL, whereas advSCs, SFRP4-SCs, SFRP2-SCs, and TNF-SCs decreased (Fig. 8b).

4.7 Subcluster-specific transcriptional changes in FL stroma

I next performed multistep DEG analyses in NHC subclusters of MFLN and FL by monitoring differences in gene expression between mLNs and pLNs (Fig. 7a,b). I observed the greatest differences in MRCs, followed by TRCs, SMC subclusters, PCs, and FDCs (Fig. 9a). Fig. 9b exhibits the expressions of the top three DEGs upregulated in FL NHC subclusters in comparison with their MFLN counterparts. In MRCs, *CXCL13* was most remarkably upregulated and GO related to lymphocyte migration was enriched (Fig. 9b–d), suggesting that MRCs, in addition to FDCs, function in accumulation of malignant B cells[9,14]. Expression of *TNFSF13B* was significantly enhanced in FL NESCs subclusters including SFRP4-SCs and AGT-SCs (Fig. 9c). *IL15* and *HGF* expressions also tended to be elevated in some FL NESC subclusters, although this finding was not statistically significant (Fig. 9c). Notably, in some NESC subclusters, I observed marked upregulation of genes relevant to solid cancers but previously not associated with lymphomagenesis including *POSTN*, *EGFL6*, and *FAP* (Fig. 9c).

In FL BECs, *GJA4* was upregulated in arterial subclusters, ABECs and aBECs (Fig. 9b), reflective of arterial vessel development[33]. Other genes involved in blood vessel development or ECM organization were upregulated in almost all subclusters (Fig. 9d). FL HEV subclusters showed high *SELE* expression (Fig. 9b), suggestive of

inflammation and HEV activation[62,63]. Indeed, FL HEV subclusters expressed genes regulating cellular adhesion and migration (Fig. 9d). Intriguingly, expression of the tip cell markers *LY6H*, *PXDN*, *PGF*, and *LOX* was remarkably upregulated in FL tBECs (Fig. 9b), suggesting acceleration of angiogenesis. The significant decrease of the proportion of LECs in FL suggests widespread lymphatic damage. IF staining confirmed that LEC density was lower in FL compared with that in MFLNs (Fig. 9e,f). Many FL LEC subclusters also showed upregulation of heat shock genes as well as *CD74*, which reportedly functions in wound healing[64] (Fig. 9b). CD74 overexpression was confirmed in FL LECs by IF staining (Fig. 9g,h).

4.8 Landscape of intercellular interactions in FL stroma

To assess the NHC/malignant B-cell crosstalk underlying FL growth, I performed scRNA-seq of cryopreserved CD45-positive cells from nine FL samples (FL 2–10) and extracted gene expression profiles of malignant B-cell clusters *in silico* from each (Fig. 10a–d).

I then performed intercellular ligand-receptor interaction analyses between FL NHC subclusters and malignant B cells using *CellPhoneDB*[47]. Thereafter, I extracted significant interactions that were considered upregulated in FL NHC subclusters relative to the corresponding MFLN subclusters.

I identified a total of 58 interactions, including some previously uncharacterized in FL (Fig. 11). In BECs, I noted that overexpression of JAG1, which is reportedly observed in B-cell lymphoma BECs and associated with aggressive lymphoma phenotypes[65], was limited to only larger arterial BEC subclusters (ABECs and caBECs) (Fig. 11). Interactions mediated through adhesion molecules, including SELE–CD44 interaction[66,67], were activated mainly in HEV subclusters (C-aHEVs, aHEVs, and hHEVs) (Fig. 11), suggestive of possible contributions of these HEV subclusters to haematogenous expansion of FL cells[66,68]. Interactions promoting cancer cell death and mediated by TNFSF10 were markedly upregulated in several LEC subclusters (Fig.

11)[69], suggesting LECs may antagonize lymphoma development. In NESCs, interactions associated with TNF signalling, cell adhesion, PDGF signalling, and chemokine signalling were differentially activated among subclusters (Fig. 11). Notably, overexpression of CXCL12, which reportedly supports FL cell migration, adhesion, and activation[70], was observed in advSCs (Fig. 11). Additionally, interactions via BAFF were upregulated, even in medullary SCs (SFRP4-SCs), suggesting stromal remodelling in FL that support extra-follicular expansion of malignant B cells[71]. In advSCs and medullary SC subclusters, interactions mediated by stroma-derived CD70 were enhanced (Fig. 11). Interactions mediated through PDGFRB, which promotes cell migration and angiogenesis[72], were enhanced in TRCs and PCs (Fig. 11), suggesting that during FL expansion mechanisms other than CCR7–CCL19/CCL21 signalling may drive homing of malignant B cells to the T-cell zone[73]. Instead, the CCR7–CCL19 interaction was extended to non-TRC SCs (TNF-SCs and PCs) (Fig. 11). Consistent with the DEG analyses of MFLN and FL, the CXCL13–CXCR5 axis[9,14] was activated in MRCs and FDCs (Fig. 11).

4.9 Enhanced CD70–CD27 interaction across FL stroma

Based on the above interactome analysis results, I next sought to explore an interaction that can potentially be targeted in lymphoma research. I carefully surveyed candidate interactions from the perspective of novelty in the field. Finally, I noted that the CD70–CD27 interaction in solid and haematologic cancers has attracted increasing attention[74-77], whereas interactions mediated by stroma-derived CD70 have rarely been investigated. Accordingly, I focused on the CD70–CD27 interaction for functional validation to verify the usefulness of our atlas-based analyses and to propose a potential mechanism in the stroma relevant to FL progression. Initially, I confirmed an overexpression of CD70 in FL medullary and adventitial SCs by IF staining (Fig. 12a,b). I next examined the gene and protein expressions of the CD70 ligand, CD27, in the B cells of FL samples. Single-cell transcriptomic analysis of FL B cells showed that *CD27* was significantly upregulated in malignant B cells compared with non-malignant B cells (Fig. 12c). Consistent with these results, flow cytometric analysis of FL haematopoietic cells showed that the $CD19^{+}CD10^{+}$ cell population (malignant B-cell enriched fraction) in five (62.5%) out of eight biologically independent samples was positive for CD27, and its expression was also significantly higher in the $CD19^{+}CD10^{+}$ population than in the $CD19^{+}CD10^{-}$ population (non-malignant B-cell fraction) (Fig.

12d,e). Among the five CD27-positive FL samples, four (80.0%) showed unequivocal binding to recombinant human CD70-Fc protein (Fig. 12f). The binding of malignant B-enriched cells to CD70-Fc protein was significantly inhibited by the treatment of the cells with an anti-CD27 function-blocking antibody in all four cases (Fig. 12f,g). Next, I performed *ex vivo* cell adhesion assays using FL frozen sections and malignant B-enriched cells. I found that the number of malignant B-enriched cells adhered to the medullary regions was significantly decreased following treatment with the anti-CD27 antibody (Fig. 12h,i).

4.10 Prognostic implications of stroma-derived markers in FL

Next, I tested the applicability of our single-cell analysis of NHCs in searching for clinically relevant factors. To correlate niche- or subcluster-specific alterations in NHCs with FL patient survival, I utilised a bulk microarray dataset of 180 biopsied FL samples from newly diagnosed patients with available survival information[48].

I narrowed down multivariate analysis candidates to seven genes (*LY6H*, *LOX*, *PTGIS*, *TDO2*, *REM1*, *PIEZO2*, and *CHI3L1*) expressed at minimal levels in FL haematopoietic cells but at high levels in FL BEC or NESC subclusters compared with MFLN counterparts. I hypothesized that they likely were associated with unfavourable prognosis (Fig. 13a–e).

In multivariate analysis, elevated expression of the tip cell markers *LY6H* and *LOX,* as well as *TDO2* and *REM1,* were shown to have unfavourable prognostic impact, even after adjustment for International Prognostic Index (Fig. 14a,b)[78]. I tested the prognostic value of the markers proposed in my analyses (*LY6H*, *LOX*, *TDO2*, and *REM1*) in the intermediate prognosis group of FL. Notably, I found that elevated *LOX* and *TDO2* expressions were prognostic even in the intermediate prognosis group, while the prognostic efficiency of *LY6H* expression was slightly not significant and that of *REM1* expression was not prognostic (Fig. 14c).

For each of the four genes, I performed IF staining in MFLN and FL samples. Cells expressing LY6H, LOX, TDO2, or REM1 were increased in FL compared with those in MFLNs (Fig. 14d).

Since these prognostic markers were derived primarily from TRCs or tBECs, I developed a FL TRC signature and evaluated its prognostic proficiency. However, I could not extract sufficient number of genes for developing a FL tBEC signature. As a result, I observed no significant difference in the overall survival of patients with high and low FL TRC signature (data not shown).

The upregulation of tip cell markers (*LY6H* and *LOX*) was prognostic in FL (Fig. 14a,b), suggesting that enhanced tumour angiogenesis might affect FL prognosis, hence I also examined the prognostic impact of conventional pan-BEC markers, *PECAM1* and *CDH5*[79]. However, I did not detect any adverse prognostic impact of these markers in the microarray dataset[48] (Fig. 14e).

4.11 Observation of NHC subclusters across lymphomas

Finally, I examined whether our single-cell atlas was applicable to different lymphoma subtypes. I also aimed to observe a more aggressive FL stromal remodelling phenotype. To this end, I performed scRNA-seq of stroma-enriched cells from five and three nodal PTCL and tDLBCL samples, respectively (Table 3; Fig. 1).

Unsupervised clustering analysis of integrated MFLN and lymphoma NHC data detected almost all NHC subclusters in both PTCL and tDLBCL (Fig. 15a–d). Furthermore, I found that BECs and LECs in these lymphomas consistently increased and decreased, respectively, as observed in FL (Fig. 15b,d). tDLBCL BECs contained abundant arterial subclusters and CXCL10-HEVs (Fig. 15d), suggesting accelerated angiogenesis and elevated HEV activities. Furthermore, I observed considerable alterations in the tDLBCL NESC proportions compared with the MFLN counterparts: the proportion of advSCs, medullary SCs, TNF-SCs, C7-SCs, AGT-SCs, and TRCs decreased considerably, whereas that of FSCs (MRCs and FDCs) increased drastically in tDLBCL, and the perivascular cell subcluster compositions remained relatively comparable (Fig. 15d). Representative DEGs upregulated in FL subclusters, including *LY6H* and *LOX* at tBECs, *SELE* at HEV subclusters, and *VCAM1* at FSCs, were also observed in tDLBCL stroma (Fig. 15e). Some key DEGs were, however, not validated,

probably because of the small sample size of tDLBCL cohort. In line with the findings of analyses on MFLN and FL NESCs, trajectories in tDLBCL NESCs indicated that non-FSC subclusters had differentiated into FSCs (Fig. 15f–h).

5. Discussion

Here, I present a human LNNHC map at single-cell resolution that was useful for exploring changes in lymphoma NHCs.

Our work sheds light on differences in mouse and human LNNHC heterogeneity. Overall, our findings suggest that human LNs harbour unique NHC subpopulations which have not been detected in murine LNs, emphasizing the need for further human studies. Although mice exhibit one HEV cluster in LNs[26], human LN HEVs were comprised of three subclusters (aHEVs, hHEVs, and CXCL10-HEVs). aHEVs expressed stress-related genes, including those associated with heat shock proteins, NFkB activation, JNK activation, and shear stress, suggesting a response to active cell deformation or damage. Some suggest that a subset of HEVs express *CXCL10*, which facilitates trafficking of activated T cells and monocytes across HEVs[40,80], though others have not detected *CXCL10* mRNA in HEVs[81]. Therefore, the CXCL10 function in HEVs remains unclear[82]. Mouse LNs have a BEC subpopulation with highly similar phenotypes to CXCL10-HEVs that exhibit a prominent interferon signalling signature, although they were classified as capillary BECs[26]. Although some degree of correlation was detected between mouse and human LN NESCs, I observed more complicated

heterogeneity in human LN NESCs than in mouse LNs and found that mouse NESC markers were not necessarily specific to human NESC counterparts.

I also observed several differences in LEC atlases between our analysis and previous analyses[23,24]. First, our analysis detected a subcluster in which gene expression patterns matched those seen in bLECs, a cell type proposed by Xiang et al (e.g. intermediate *BMP2* expression between cLECs and fLECs)[24], although bLECs were not detected by Takeda et al[23]. Second, I initially could not identify fLECs and pfsLECs as distinct subclusters[23,24]. Lastly, two valve LEC subclusters (Up- and Down-valves) were identified as distinct, in contrast to a previous study that identified them after applying sub-clustering analysis to an initially-identified valve cluster (LEC V)[23]. I speculate that these inconsistencies are due to the fact that previous studies collected LEC-enriched cells based on PDPN positivity in flow cytometric analysis, and thus LECs with relatively low PDPN expression may have been overlooked. Indeed, *PDPN* expression was particularly low in bLECs and down-valves.

As in the previous studies that required fresh human LN samples[23,27], I used MFLNs from tumour-bearing patients for atlas construction. Notably, detailed analysis of LNNHCs from a patient with a benign tumour indicated that the clustering was comparable between samples from benign tumour- and malignancy-bearing patients.

This observation suggests minimal or negligible influence of malignancy-derived factors on our atlas. I also profiled DEGs between mLN and pLN NHC subclusters using MFLN data. Our data were consistent with MADCAM1-dependent manners of lymphocyte homing in mLN HEVs[40] and the constant exposure of mLNs LEC and NESC subclusters to enterobacteria-derived factors.

Multistep DEG analyses revealed subcluster-specific changes in FL, including those with a previously unknown function in lymphoma. *POSTN* encodes periostin, a protein secreted by cancer-associated fibroblasts (CAFs) that promotes formation of cancer stem cell, perivascular, and premetastatic niches[83]. *EGFL6* encodes EGFL6, a member of the EGF-like superfamily that reportedly promotes tumour cell growth by stimulating angiogenesis[84,85]. These mechanisms may function in lymphoma stroma. CAFs positive for fibroblast activation protein are associated with an immunosuppressive environment, which hampers immunotherapy[86-88]. Intriguingly, *FAP* was most upregulated in FSCs (MRCs and FDCs), indicating that in FL FSCs may create an immunological environment favouring malignant cells.

Remarkably, I found that upregulation of some known intercellular interactions across FL NHCs and malignant B cells was extended to unanticipated NHC subclusters and, conversely, other interactions were enhanced in limited NHC subclusters. These

observations largely increase the resolution of our understating of stromal remodelling in lymphoma. Additionally, these findings may be of clinical importance, suggesting potential stroma-derived prognostic factors. Notably, two tip cell markers were upregulated in FL and could potentially serve as prognostic factors. LOX enzymatic activity reportedly drives tumour angiogenesis by activating PDGFRβ signalling in vascular SMCs, consistent with our findings in DEG analysis that FL SMCs highly expressed *PDGFRB*[89]. Meanwhile, our observation of *LY6H* expression in tip cells has not previously been described in mouse or human endothelial cells. I also identified *TDO2* as a prognostic predictor of FL. *TDO2* may function to attract regulatory T cells, antagonize CD8+ T cell activity, and accelerate myeloid cell tolerogenicity[90]. *REM1* overexpression in TRCs and PCs was also associated with unfavourable FL outcomes. Thus, further analysis of this gene, which has been scarcely explored, and its relevance to the lymphoma stroma is warranted. Since the enrichment of FL TRC signature per se was not prognostic, qualitative rather than quantitative alterations in certain NHC subpopulations may affect the chemoresistance and prognosis of FL more precisely. Besides these prognostic factors, many upregulated genes with or without a known pro-tumorigenic function were included in our dataset, making our atlas a powerful discovery tool for additional therapeutic targets.

Third, I found that the CD70–CD27 interaction via stroma-derived CD70 was enhanced in FL. Although the role of CD70 has increasingly been investigated in the context of interplays across various immune cells and cancer cells[76,77], lymphoma SCs have not been explored as a source of CD70. A recent report suggested that CD70 expressed by CAFs supports tumour progression in solid cancers by facilitating cancer cell migration[91]. Consistent with these findings, I confirmed binding between CD70 and malignant B cells that could be blocked by an antagonist against CD70 ligand, CD27. CD70 was upregulated in extrafollicular FL SCs, suggesting that CD70 may facilitate infiltration of lymphoma cells into extrafollicular regions during tumour progression. Our analysis thus proposed stroma-derived CD70 as a potential biomarker and therapeutic target of FL.

Lastly, I found that NHC heterogeneities in LNs were detectable even in aggressive lymphomas, confirming the usefulness of our NHC atlas in characterizing stroma of various lymphoma subtypes. Particularly, alterations in tDLBCL stroma harmonized with those in FL, supporting the findings in analysis of FL stroma. Furthermore, our findings indicate that extra-follicular SCs, including TRCs and medullary SCs, not only promote extra-follicular infiltration of FL cells, but simultaneously differentiate into FSCs and finally are replaced by FSCs in more

advanced phenotypes, reflecting an unique stromal transition corresponding to the FSC-dependent growth manner of FL[92].

Limitations of this study include the quantity of samples, which may not be sufficient to identify all NHC subpopulations or to precisely determine the correlation between the NHC heterogeneities in the transcriptome data and patient characteristics, such as the genomic alterations. Second, I cannot completely exclude the possibility that our atlas is somewhat influenced by unknown factors from distant malignancy. Third, our study was not designed to analyse other lymphoma subtypes or non-lymphoma diseases. Finally, further functional validation is required to confirm our findings relevant to each NHC subcluster.

6. Conclusion

Here, I developed and validated a single-cell atlas of NHCs in human LNs and lymphoma.The atlas is of great value to lymphoma researchers, as it largely updates the NHC taxonomy in human LNs in the context of lymphoma research. This study provides a platform for future research aiming at deeper understanding of LN or lymphoma biology and at improving lymphoma management.

7. Figures

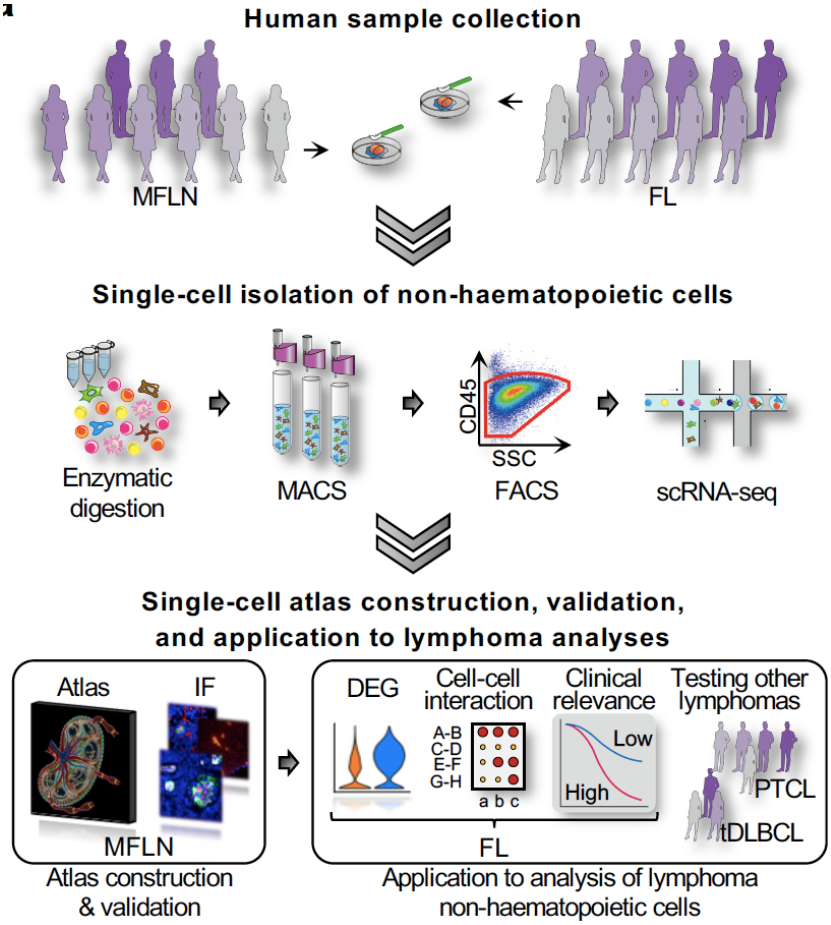

Figure 1.

Study overview showing experimental and analytical workflows. DEG, differentially expressed gene; FACS, fluorescence-activated cell sorting; IF, immunofluorescence; MACS, magnetic-activated cell sorting; MFLN, metastasis-free lymph node; PTCL, peripheral T-cell lymphoma; tDLBCL, diffuse large B-cell lymphoma transformed from FL.

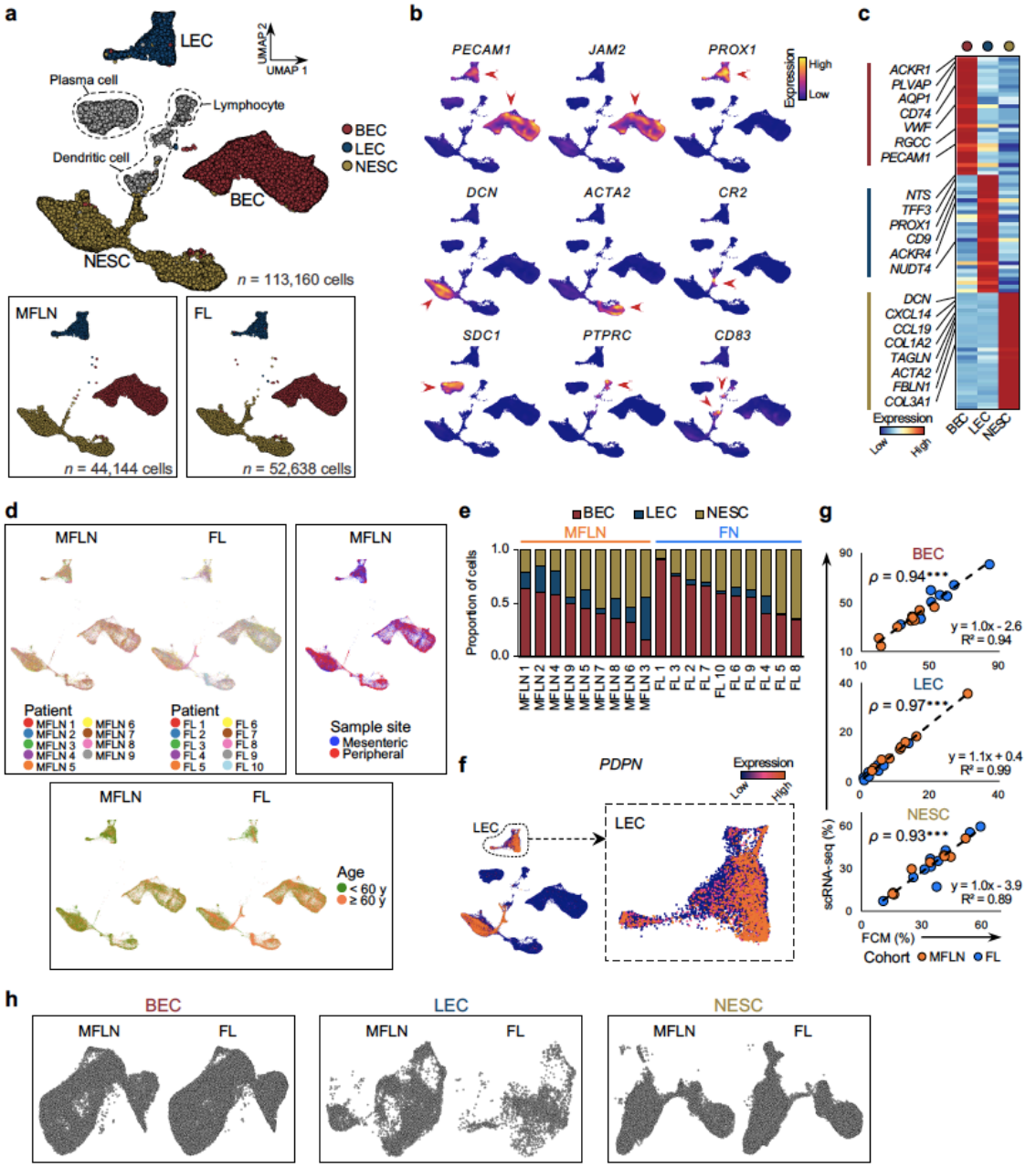

Figure 2.

a, UMAP plots of stroma-enriched cells from nine human MFLN and ten FL samples, coloured by cell type (top panel). Major non-haematopoietic cell (NHC) components from MFLN and FL samples are shown separately (bottom left and bottom right, respectively). BEC, blood endothelial cell; LEC, lymphatic endothelial cell; NESC, non-endothelial stromal cell.

b, Expression of marker genes used to identify cell types. Red arrowheads show cells expressing indicated marker genes.

c, Heatmap showing expression of top-ranking marker genes for each major NHC component. Key genes are indicated on the left.

d, UMAP plots of NHCs, colour coded by patients (top left), sites of sample collection (top right), and patient age (bottom), according to patient cohorts.

e, Proportion of each major NHC component between MFLN (left) and FL (right) cohorts.

f, *PDPN* expression in stroma-enriched cells from MFLN samples. High magnification image indicates heterogeneous *PDPN* expression levels among LECs.

g, Correlation of proportions of BECs (top), LECs (middle), and NESCs (bottom) among stroma-enriched cells, as evaluated using flow cytometric (FCM) analysis and scRNA-seq; coloured according to patient cohort. Circles indicate biologically independent samples (MFLN; $n = 9$, FL; $n = 10$). ρ denotes Spearman's rank correlation coefficient. ***$P = 4.0 \times 10^{-6}$ (BEC), ***$P = 8.0 \times 10^{-6}$ (LEC), ***$P = 2.5 \times 10^{-6}$ (NESC) (two-sided Spearman's rank correlation test).

h, UMAP plots of LN BECs (left), LECs (middle), and NESCs (right) after re-clustering analysis shown according to patient cohort (MFLN or FL cohort in left or right panel in each component, respectively).

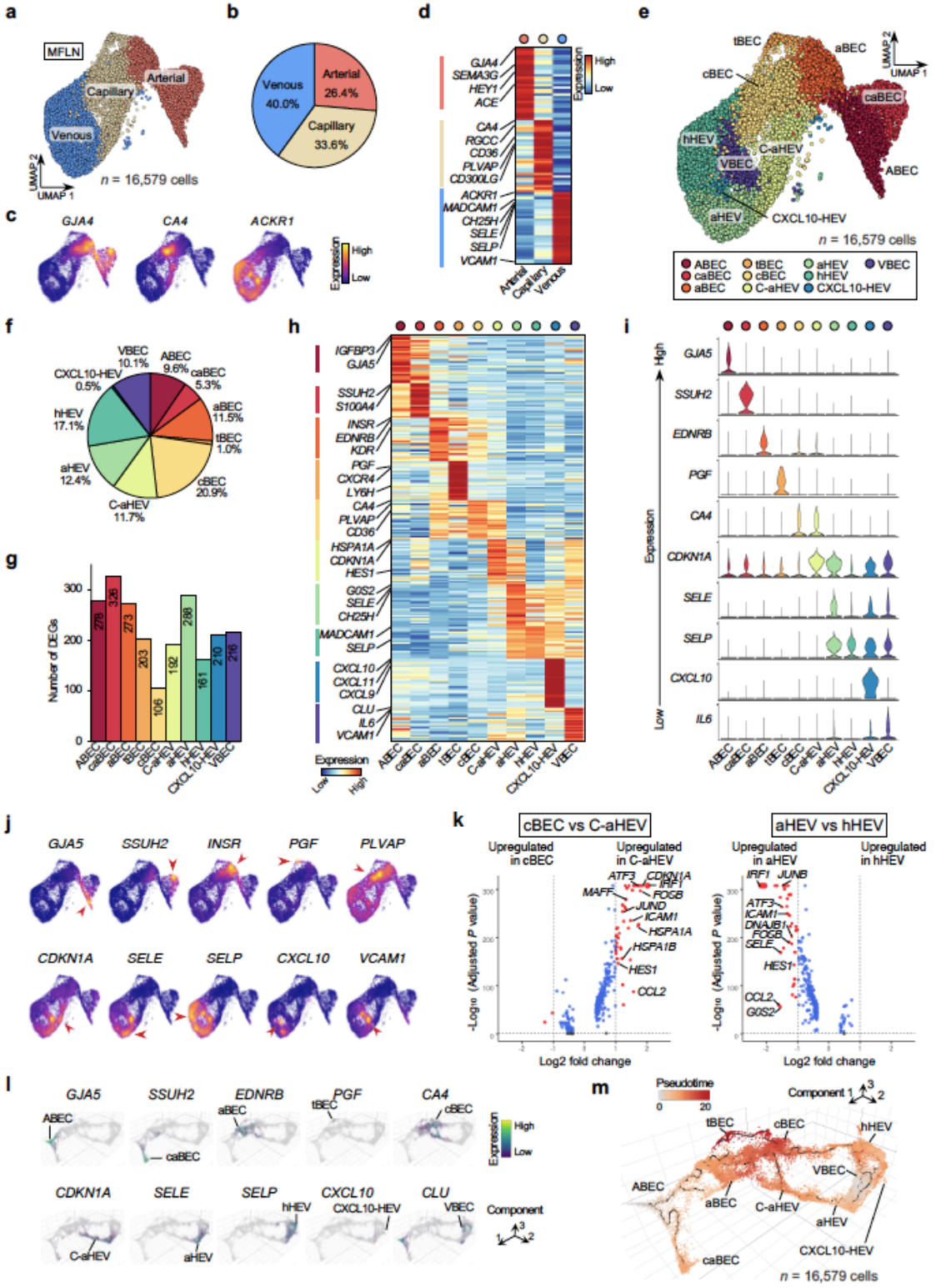
a
MFLN
Arterial
Capillary
Venous
n = 16,579 cells
UMAP 1
UMAP 2
b
Arterial 26.4%
Capillary 33.6%
Venous 40.0%
c
GJA4
CA4
ACKR1
High
Low
Expression
d
GJA4
SEMA3G
HEY1
ACE
CA4
RGCC
CD36
PLVAP
CD300LG
ACKR1
MADCAM1
CH25H
SELE
SELP
VCAM1
Arterial
Capillary
Venous
e
tBEC
aBEC
cBEC
caBEC
hHEV
C-aHEV
VBEC
ABEC
aHEV
CXCL10-HEV
n = 16,579 cells
ABEC
caBEC
aBEC
tBEC
cBEC
C-aHEV
aHEV
hHEV
CXCL10-HEV
VBEC
f
VBEC 10.1%
ABEC 9.6%
caBEC 5.3%
aBEC 11.5%
tBEC 1.0%
cBEC 20.9%
C-aHEV 11.7%
aHEV 12.4%
hHEV 17.1%
CXCL10-HEV 0.5%
g
Number of DEGs
278
326
273
203
106
192
288
161
210
216
h
IGFBP3
GJA5
SSUH2
S100A4
INSR
EDNRB
KDR
PGF
CXCR4
LY6H
CA4
PLVAP
CD36
HSPA1A
CDKN1A
HES1
GOS2
SELE
CH25H
MADCAM1
SELP
CXCL10
CXCL11
CXCL9
CLU
IL6
VCAM1
Expression
Low
High
i
GJA5
SSUH2
EDNRB
PGF
CA4
CDKN1A
SELE
SELP
CXCL10
IL6
High
Low
Expression
j
GJA5
SSUH2
INSR
PGF
PLVAP
CDKN1A
SELE
SELP
CXCL10
VCAM1
k
cBEC vs C-aHEV
aHEV vs hHEV
Upregulated in cBEC
Upregulated in C-aHEV
Upregulated in aHEV
Upregulated in hHEV
ATF3
CDKN1A
IRF1
FOSB
MAFF
JUND
ICAM1
HSPA1A
HSPA1B
HES1
CCL2
IRF1
JUNB
ATF3
ICAM1
DNAJB1
FOSB
SELE
HES1
CCL2
GOS2
-Log10 (Adjusted P value)
Log2 fold change
l
GJA5
SSUH2
EDNRB
PGF
CA4
ABEC
caBEC
aBEC
tBEC
cBEC
High
Low
Expression
CDKN1A
SELE
SELP
CXCL10
CLU
C-aHEV
aHEV
hHEV
CXCL10-HEV
VBEC
Component
m
Pseudotime
0
20
Component 1
2
3
tBEC
cBEC
hHEV
VBEC
ABEC
aBEC
C-aHEV
aHEV
CXCL10-HEV
caBEC
n = 16,579 cells

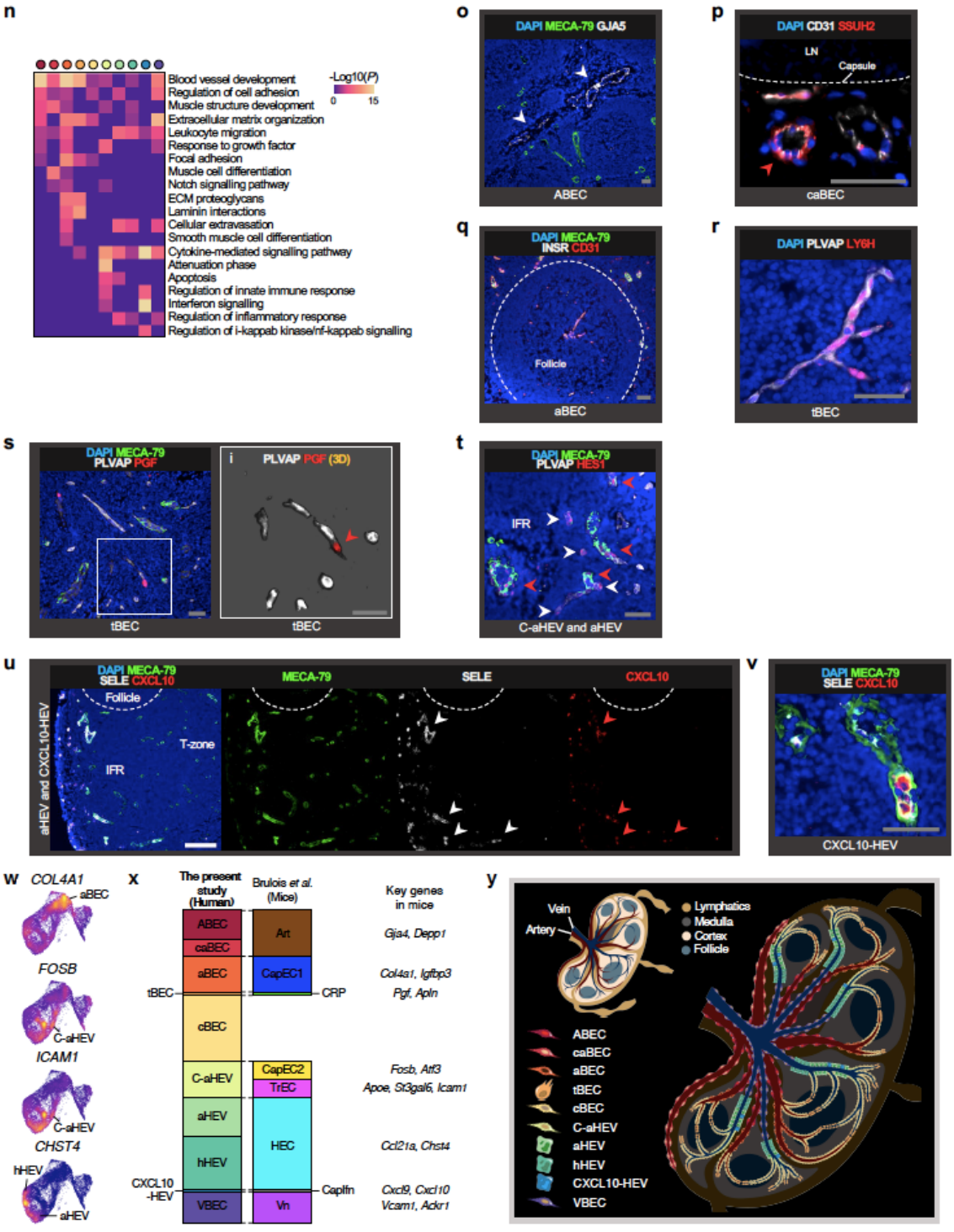

Figure 3.

a, UMAP plot of MFLN BECs, coloured according to classification of arterial, capillary, and venous BECs.

b, Proportions of arterial, capillary, and venous BECs in MFLN samples.

c, Expression of arterial, capillary, and venous BEC marker genes.

d, Heatmap showing expression of top-ranking marker genes of arterial, capillary, and venous BECs. Key genes are indicated on the left.

e, UMAP plot of 10 MFLN BEC subclusters identified by unsupervised clustering.

f, Prevalence of each BEC subcluster in MFLN samples.

g, Number of DEGs per BEC subcluster.

h, Heatmap showing expression of top-ranking marker genes for each BEC subcluster. Key genes are indicated on left.

i, Violin plots representing expression of top marker genes for each BEC subcluster.

j, Expression of marker genes for each BEC subcluster. Red arrowheads show cells expressing indicated marker genes.

k, Volcano plots of up- or down-regulated genes between cBECs and C-aHEVs (left) or between aHEVs and hHEVs (right). Significance was determined as an adjusted P value of <0.05 (two-sided Wilcoxon Rank-Sum test with Bonferroni correction) (blue-coloured dots) and log2 fold-change of ≥ 1 (red-coloured dots). Larger dots indicate log2 fold-change of ≥ 2. Key genes are labelled.

l, Expression of marker genes for each BEC subcluster in a single-cell BEC object, generated by

Monocle 3.

m, Single-cell BECs ordered according to pseudo-time developmental stages. Dark winding lines in the cell object indicate putative developmental trajectories. Cell regions are assigned to BEC subclusters based on subcluster-defining gene expressions.

n, GO enrichment analysis of DEGs for each BEC subcluster.

o, IF staining of MECA-79 (green) and GJA5 (white) shows large arterial BECs (ABECs) (white arrowheads).

p, CD31 (white) and SSUH2 (red) identify arteries surrounding LN capsule (caBECs) (red arrowhead).

q, MECA-79 (green), INSR (white), and CD31 (red) identify arterioles (aBECs).

r, PLVAP (white) and LY6H (red) (top left) to identify tBECs.

s, MECA-79 (green), PLVAP (white), and PGF (red). High magnification image is presented in 3D identifying tip cells (tBECs).

t, MECA-79 (green), PLVAP (white), and HES1 (red) show activated HEVs (aHEVs) (red arrowheads) and transitional BECs between capillary BECs and aHEVs (C-aHEVs) (white arrowheads).

u, MECA-79 (green), SELE (white), and CXCL10 (red) to identify CXCL10-HEVs.

v, MECA-79 (green), SELE (white), and CXCL10 (red) to discriminate aHEVs from hHEVs and

to identify CXCL10-HEVs.

Scale bars, 50 μm (grey), 200 μm (white).

w, Expression of marker genes for key mouse LN BEC subclusters (proposed by Brulois et al[26]) in our human data.

x, Comparison of BEC subclusters identified here with those characterized in mice[26]. Bar heights of the mouse study are adjusted to the cell numbers (belonging to each subcluster) identified in this study. Key markers for mouse BEC subclusters[26] are listed on right.

y, LN schematic depicting topological localization of 10 BEC subclusters.

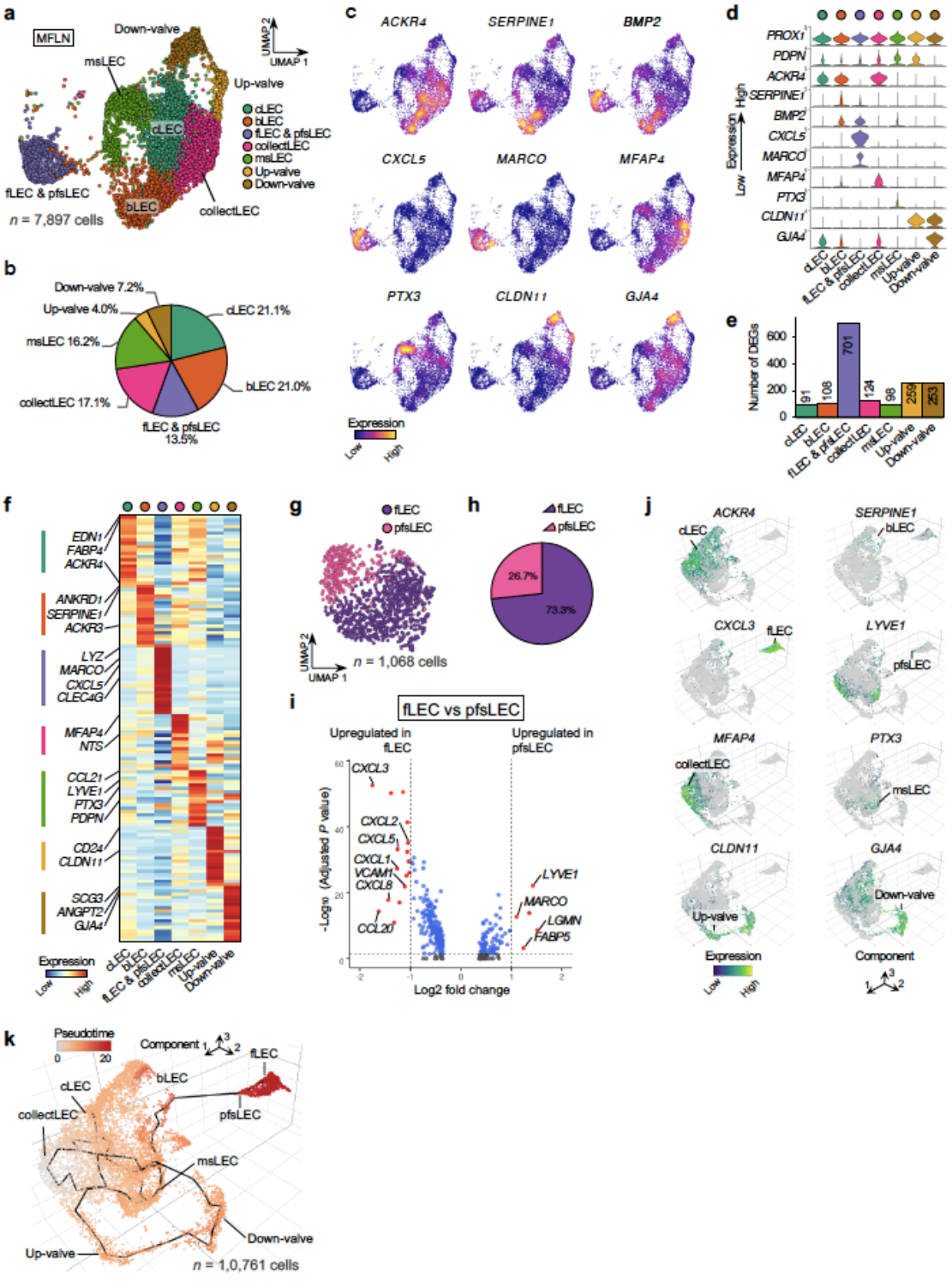
a
MFLN
Down-valve
msLEC
Up-valve
cLEC
bLEC
fLEC & pfsLEC
collectLEC
msLEC
Up-valve
Down-valve
UMAP 2
UMAP 1
fLEC & pfsLEC
bLEC
collectLEC
n = 7,897 cells
b
Down-valve 7.2%
Up-valve 4.0%
cLEC 21.1%
msLEC 16.2%
bLEC 21.0%
collectLEC 17.1%
fLEC & pfsLEC 13.5%
c
ACKR4
SERPINE1
BMP2
CXCL5
MARCO
MFAP4
PTX3
CLDN11
GJA4
Expression
Low
High
d
PROX1
PDPN
ACKR4
SERPINE1
BMP2
CXCL5
MARCO
MFAP4
PTX3
CLDN11
GJA4
High
Expression
Low
cLEC
bLEC
fLEC & pfsLEC
collectLEC
msLEC
Up-valve
Down-valve
e
Number of DEGs
600
400
200
0
91
108
701
124
98
258
253
cLEC
bLEC
fLEC & pfsLEC
collectLEC
msLEC
Up-valve
Down-valve
f
EDN1
FABP4
ACKR4
ANKRD1
SERPINE1
ACKR3
LYZ
MARCO
CXCL5
CLEC4G
MFAP4
NTS
CCL21
LYVE1
PTX3
PDPN
CD24
CLDN11
SCG3
ANGPT2
GJA4
Expression
Low
High
cLEC
bLEC
fLEC & pfsLEC
collectLEC
msLEC
Up-valve
Down-valve
g
fLEC
pfsLEC
UMAP 2
UMAP 1
n = 1,068 cells
h
fLEC
pfsLEC
26.7%
73.3%
i
fLEC vs pfsLEC
Upregulated in fLEC
Upregulated in pfsLEC
-Log10 (Adjusted P value)
CXCL3
CXCL2
CXCL5
CXCL1
VCAM1
CXCL8
CCL20
LYVE1
MARCO
LGMN
FABP5
Log2 fold change
j
ACKR4
cLEC
SERPINE1
bLEC
CXCL3
fLEC
LYVE1
pfsLEC
MFAP4
collectLEC
PTX3
msLEC
CLDN11
Up-valve
GJA4
Down-valve
Expression
Low
High
Component
k
Pseudotime
0
20
Component
fLEC
bLEC
cLEC
collectLEC
pfsLEC
msLEC
Down-valve
Up-valve
n = 1,0,761 cells

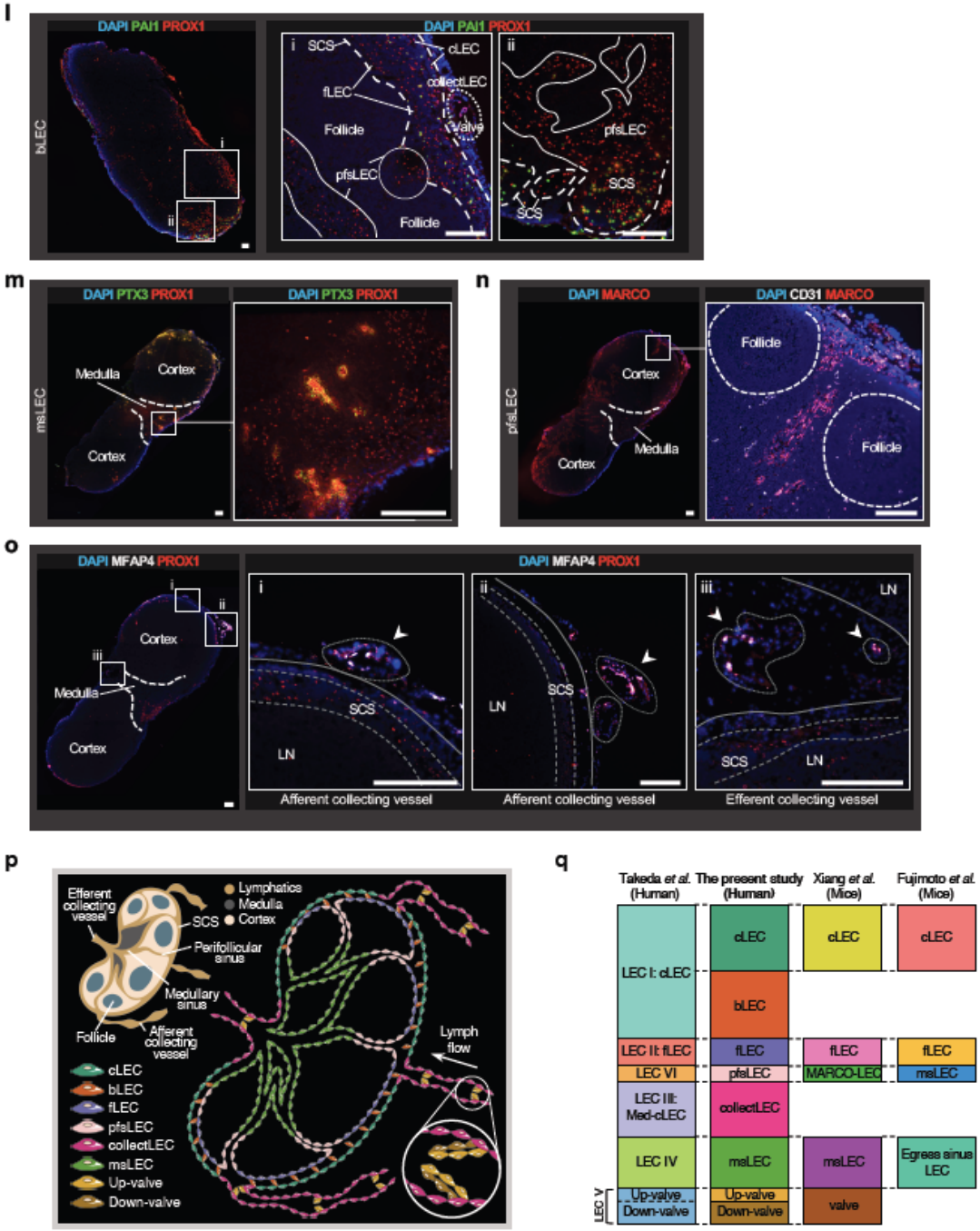

Figure 4.

a, UMAP plot of MFLN LEC subclusters identified by unsupervised clustering.

b, Prevalence of each LEC subcluster in MFLN samples.

c, Expression of marker genes for each LEC subcluster.

d, Violin plots showing expression of top marker genes for each LEC subcluster.

e, Number of DEGs per LEC subcluster.

f, Heatmap showing expression of top-ranking marker genes for each LEC subcluster. Key genes are indicated on the left.

g, UMAP plot of fLECs and pfsLECs discriminated by unsupervised sub-clustering of a single "fLEC and pfsLEC" subcluster.

h, Composition of fLECs and pfsLECs in the "fLEC and pfsLEC" subcluster.

i, Volcano plot of up- or down-regulated genes in fLECs and pfsLECs. Significance was determined as an adjusted *P* value of <0.05 (two-sided Wilcoxon Rank-Sum test with Bonferroni correction) (blue-coloured dots) and log2 fold-change of ≥1 (red-coloured dots). Key genes are labelled.

j, Expression of marker genes for each LEC subcluster in a single-cell LEC object, generated by *Monocle 3*.

k, Single-cell LECs, ordered according to pseudo-time developmental stages. Dark winding lines indicate putative developmental trajectories. Cell regions are assigned to LEC subclusters based on marker gene expression.

l, IF staining of PAI1 (green) and PROX1 (red) to identify bridge LECs (bLECs). Scale bars, 500 μm (left panel), 200 μm (magnification panels).

m, PTX3 (green) and PROX1 (red) to identify medullary sinus LECs (msLECs). High magnification image at right corresponds to boxed area at left. Scale bars, 200 μm.

n, MARCO (red) for identification of perifollicular sinus LECs (pfsLECs). High magnification image at right shows staining of CD31 (white) and MARCO (red). Dashed lines indicate boundaries between the LN cortex and medullary regions (left) or follicles (right). Scale bars, 200 μm.

o, MFAP4 (white) and PROX1 (red) to identify collecting vessel LECs (arrowheads). High magnification images show afferent (i and ii) or efferent (iii) collecting vessels. Scale bars, 200 μm (**l**).

p, Schematic showing topological localization of eight LEC subclusters in the LN.

q, Comparison of subclusters identified here with those previously characterized[23-25]. Bar heights of the previous studies are adjusted to cell numbers (belonging to each subcluster) identified in this study.

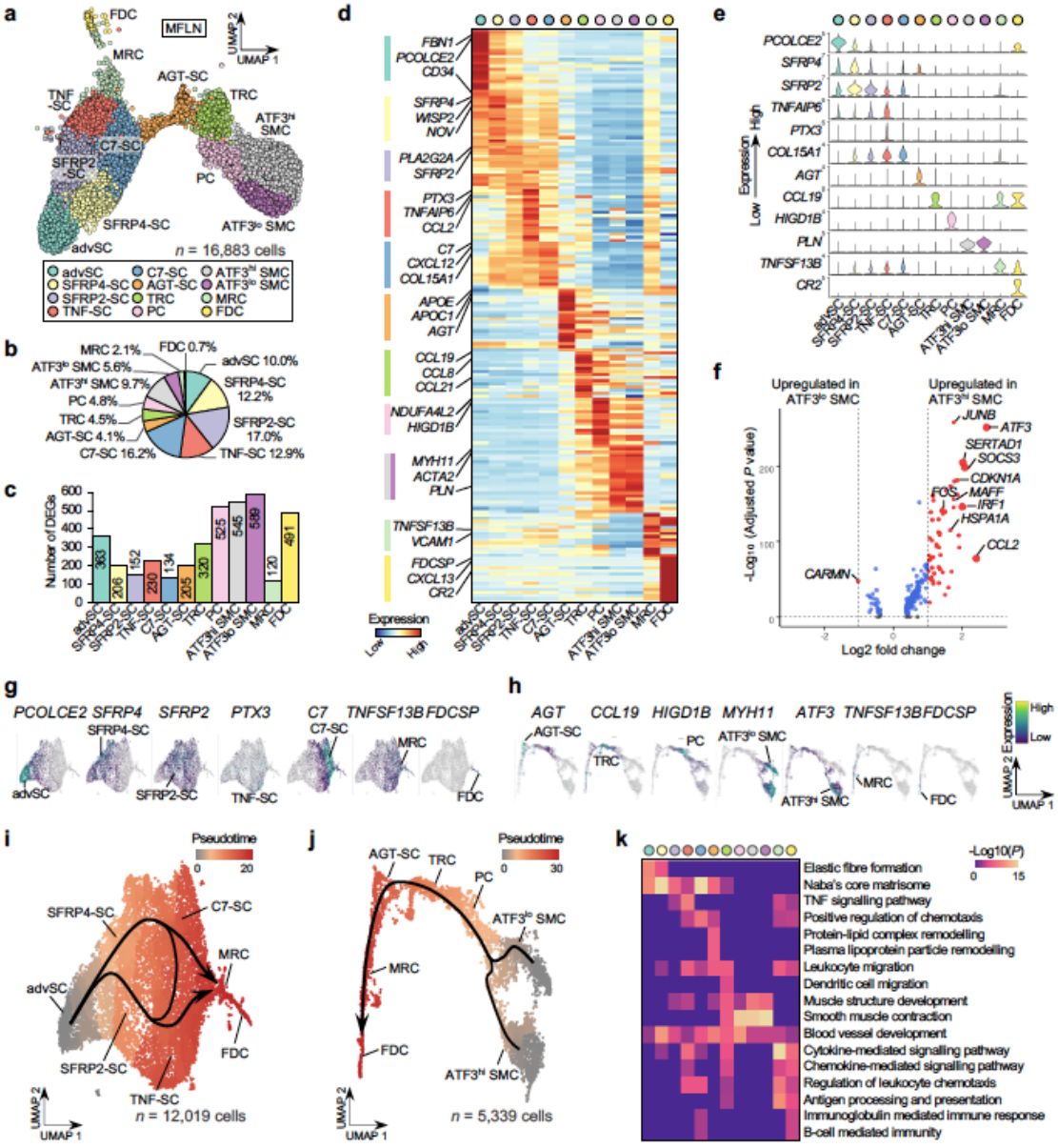
a
FDC
MFLN
MRC
AGT-SC
TRC
TNF-SC
ATF3H SMC
C7-SC
SFRP2-SC
PC
SFRP4-SC
ATF3lo SMC
advSC
n = 16,883 cells
advSC
SFRP4-SC
SFRP2-SC
TNF-SC
C7-SC
AGT-SC
TRC
PC
ATF3H SMC
ATF3lo SMC
MRC
FDC
b
MRC 2.1%
FDC 0.7%
ATF3lo SMC 5.6%
advSC 10.0%
ATF3H SMC 9.7%
SFRP4-SC 12.2%
PC 4.8%
TRC 4.5%
SFRP2-SC 17.0%
AGT-SC 4.1%
C7-SC 16.2%
TNF-SC 12.9%
c
Number of DEGs
363
206
152
230
134
205
320
525
545
589
120
461
d
FBN1
PCOLCE2
CD34
SFRP4
WISP2
NOV
PLA2G2A
SFRP2
PTX3
TNFAIP6
CCL2
C7
CXCL12
COL15A1
APOE
APOC1
AGT
CCL19
CCL8
CCL21
NDUFA4L2
HIGD1B
MYH11
ACTA2
PLN
TNFSF13B
VCAM1
FDCSP
CXCL13
CR2
Expression
Low
High
e
PCOLCE2
SFRP4
SFRP2
TNFAIP6
PTX3
COL15A1
AGT
CCL19
HIGD1B
PLN
TNFSF13B
CR2
High
Low
Expression
f
Upregulated in ATF3lo SMC
Upregulated in ATF3H SMC
JUNB
ATF3
SERTAD1
SOCS3
CDKN1A
FOS
MAFF
IRF1
HSPA1A
CCL2
CARMN
-Log10 (Adjusted P value)
Log2 fold change
g
PCOLCE2
SFRP4
SFRP2
PTX3
C7
TNFSF13B
FDCSP
SFRP4-SC
C7-SC
MRC
advSC
SFRP2-SC
TNF-SC
FDC
h
AGT
CCL19
HIGD1B
MYH11
ATF3
TNFSF13B
FDCSP
AGT-SC
PC
ATF3lo SMC
TRC
ATF3H SMC
MRC
FDC
High
Low
UMAP 2 Expression
UMAP 1
i
Pseudotime
0
20
SFRP4-SC
C7-SC
MRC
advSC
FDC
SFRP2-SC
TNF-SC
n = 12,019 cells
UMAP 2
UMAP 1
j
Pseudotime
0
30
AGT-SC
TRC
PC
ATF3lo SMC
MRC
FDC
ATF3H SMC
n = 5,339 cells
UMAP 2
UMAP 1
k
-Log10(P)
0
15
Elastic fibre formation
Naba's core matrisome
TNF signalling pathway
Positive regulation of chemotaxis
Protein-lipid complex remodelling
Plasma lipoprotein particle remodelling
Leukocyte migration
Dendritic cell migration
Muscle structure development
Smooth muscle contraction
Blood vessel development
Cytokine-mediated signalling pathway
Chemokine-mediated signalling pathway
Regulation of leukocyte chemotaxis
Antigen processing and presentation
Immunoglobulin mediated immune response
B-cell mediated immunity

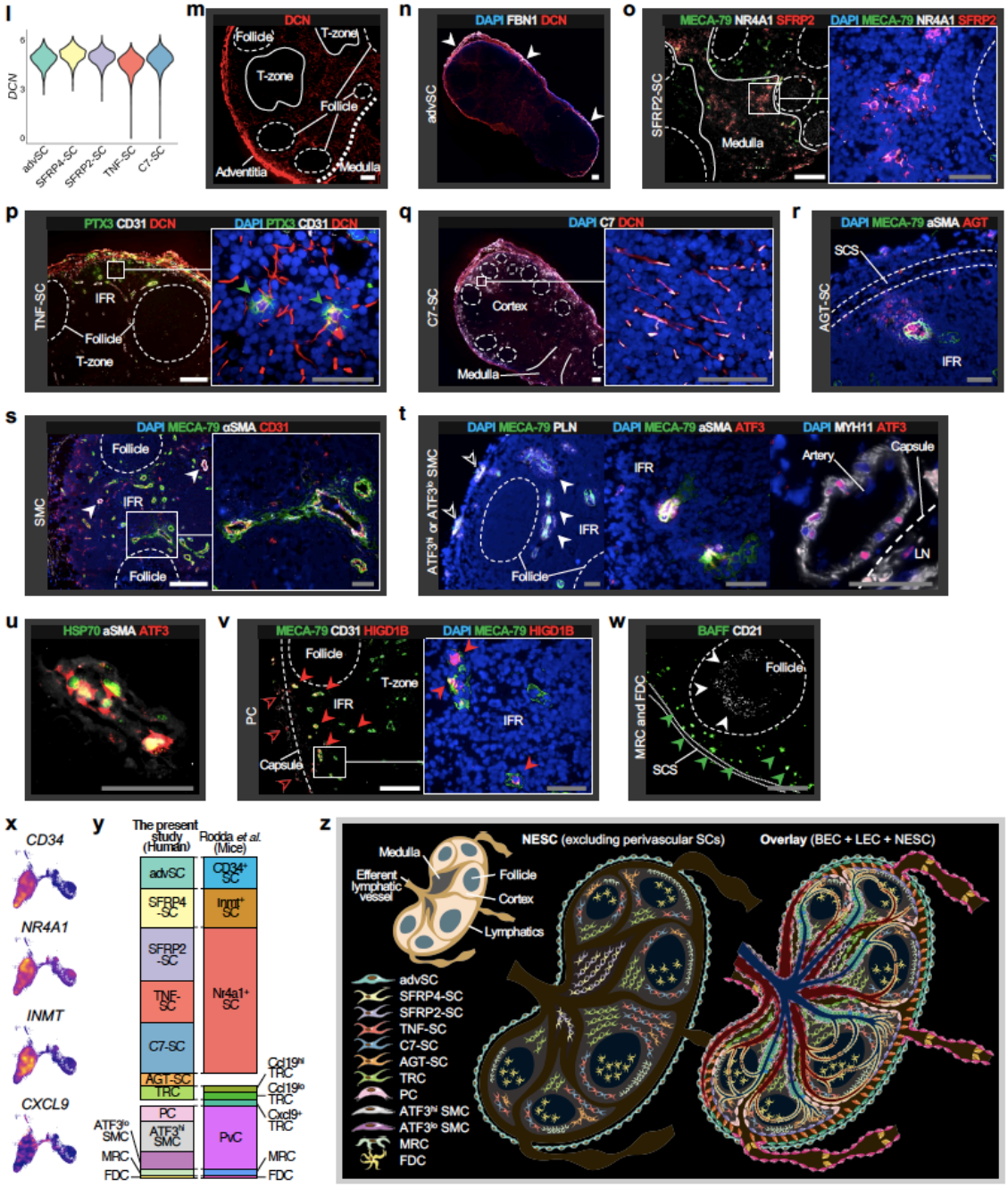

Figure 5.

a, UMAP plot of MFLN NESC subclusters identified by unsupervised clustering.

b, Prevalence of each NESC subcluster in MFLN samples.

c, Number of DEGs per NESC subcluster.

d, Heatmap showing expression of top-ranking marker genes for each NESC subcluster. Key genes are indicated on the left.

e, Violin plots representing top marker genes for each NESC subcluster.

f, Volcano plot of up- or down-regulated genes between $ATF3^{hi}$ and $ATF3^{lo}$ SMCs. Significance was determined as an adjusted *P* value of <0.05 (two-sided Wilcoxon Rank-Sum test with Bonferroni correction) (blue-coloured dots) and log2 fold-change of ≥1 (red-coloured dots). Larger dots indicate log2 fold-change of ≥2. Key genes are labelled.

g, Marker gene expressions in a NESC object shown in Fig. 5i.

h, Marker gene expressions in a NESC object shown in Fig. 5j.

i, Pseudo-time developmental stages of single cells in advSCs, SFRP4-SCs, SFRP2-SCs, TNF-SCs, C7-SCs, MRCs, and FDCs.

j, Pseudo-time developmental stages of single cells in SMC subclusters, PCs, TRCs, AGT-SCs, MRCs, and FDCs.

k, GO enrichment analysis of DEGs for each NESC subcluster.

l, *DCN* expression in MFLN advSCs, SFRP4-SCs, SFRP2-SCs, TNF-SCs, and C7-SCs.

m, IF staining of DCN showing DCN-positive fibroblasts.

n, FBN1 (white) and DCN (red) to identify SCs in the capsule adventitia (advSC) (arrowheads).

o, MECA-79 (green), NR4A1 (a marker of LN fibroblastic reticular cells; white)[22], and SFRP2

(red) to identify SFRP2-SCs.

p, PTX3 (green), CD31 (white), and DCN (red) to identify TNF-SCs (green arrowheads).

q, C7 (white) and DCN (red) to identify C7-SCs.

r, MECA-79 (green), α-smooth muscle actin (αSMA, white), and AGT (red) to identify AGT-SCs.

s, MECA-79 (green), αSMA (white), and CD31 (red) to identify SMCs. White arrowheads indicate SMCs around arteries.

t, MECA-79 (green) and PLN (white) identifying SMCs around HEVs (filled arrowheads) and arteries (empty arrowheads) (left); MECA-79 (green), αSMA (white), and ATF3 (red) identifying $ATF3^{hi}$ SMCs around HEVs (middle); and MYH11 (white) and ATF3 (red) showing $ATF3^{hi}$ and $ATF3^{lo}$ SMCs around arteries.

u, HSP70 (green), αSMA (white), and ATF3 (red) on SMCs.

v, MECA-79 (green), CD31 (white), and HIGD1B (red) identifying PCs around arteries (empty arrowheads) and HEVs (filled arrowheads).

w, BAFF (green) and CD21 (white) identifying MRCs (green arrowheads) and FDCs (white arrowheads), respectively.

Scale bars, 50 μm (grey),200 μm (white).

x, Expression of marker genes for key mouse LN NESC subclusters[22] in our human data.

y, Comparison of NESC subclusters identified here with those characterized in mice[22].

z, LN schematic depicting NESC subclusters excluding perivascular SCs (left) and an overlay image of all BEC, LEC, and NESC subclusters (right).

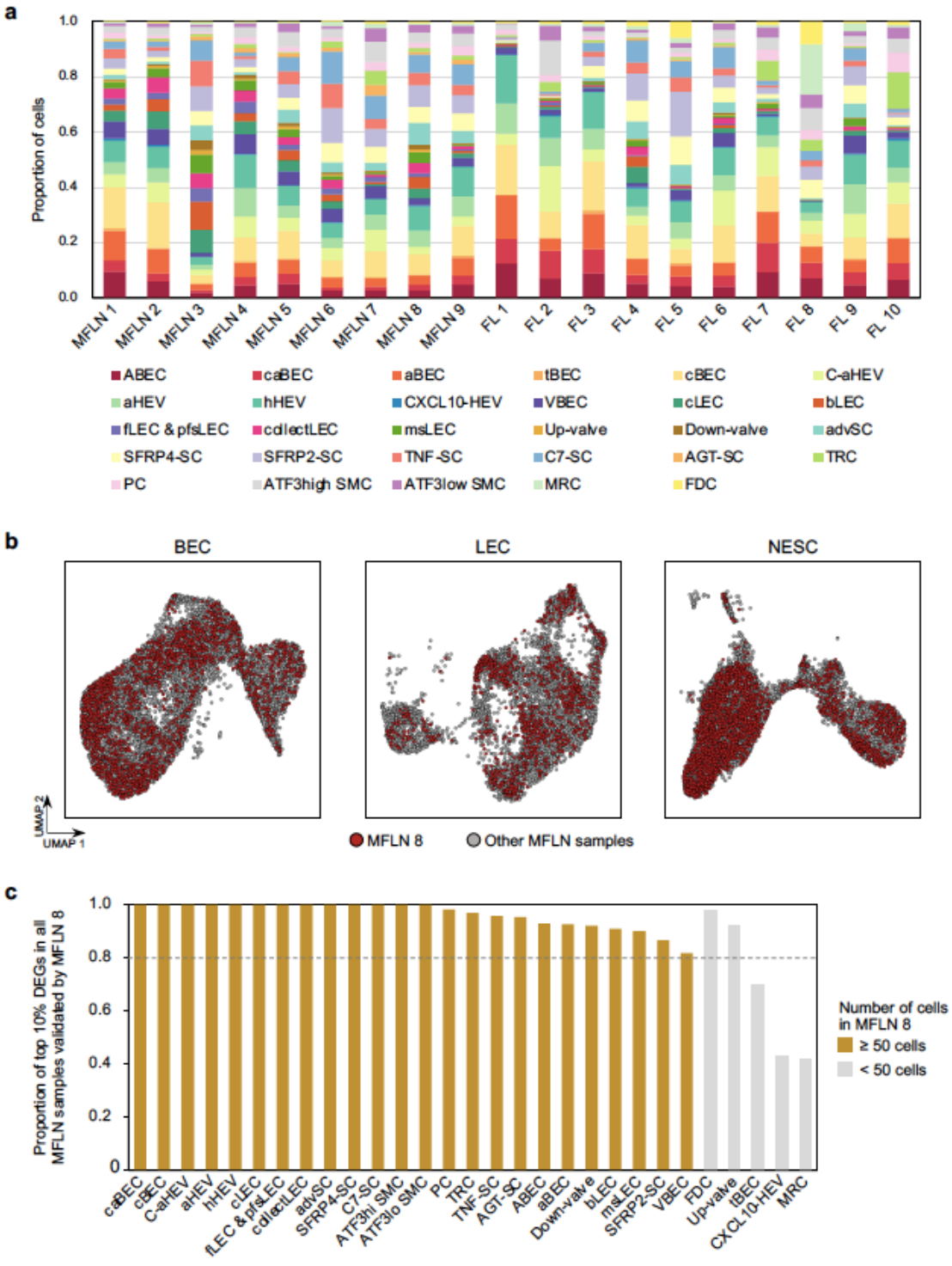

Figure 6.

a, Proportion of each NHC subcluster based on patients in the MFLN and FL cohorts.

b, UMAP plot of major NHC components from MFLN samples, highlighting NHCs from a patient

with a benign tumour (MFLN 8) (red dots).

c, Proportions of top DEGs detected using all MFLN data and validated by DEGs in MFLN 8 according to NHC subclusters. Top DEGs were defined as the top 10% of DEGs of each NHC subcluster, calculated using all MFLN data. Bars of subclusters with >50 cells in MFLN 8 were highlighted by ochre colouring. Dashed line indicates 80% validation.

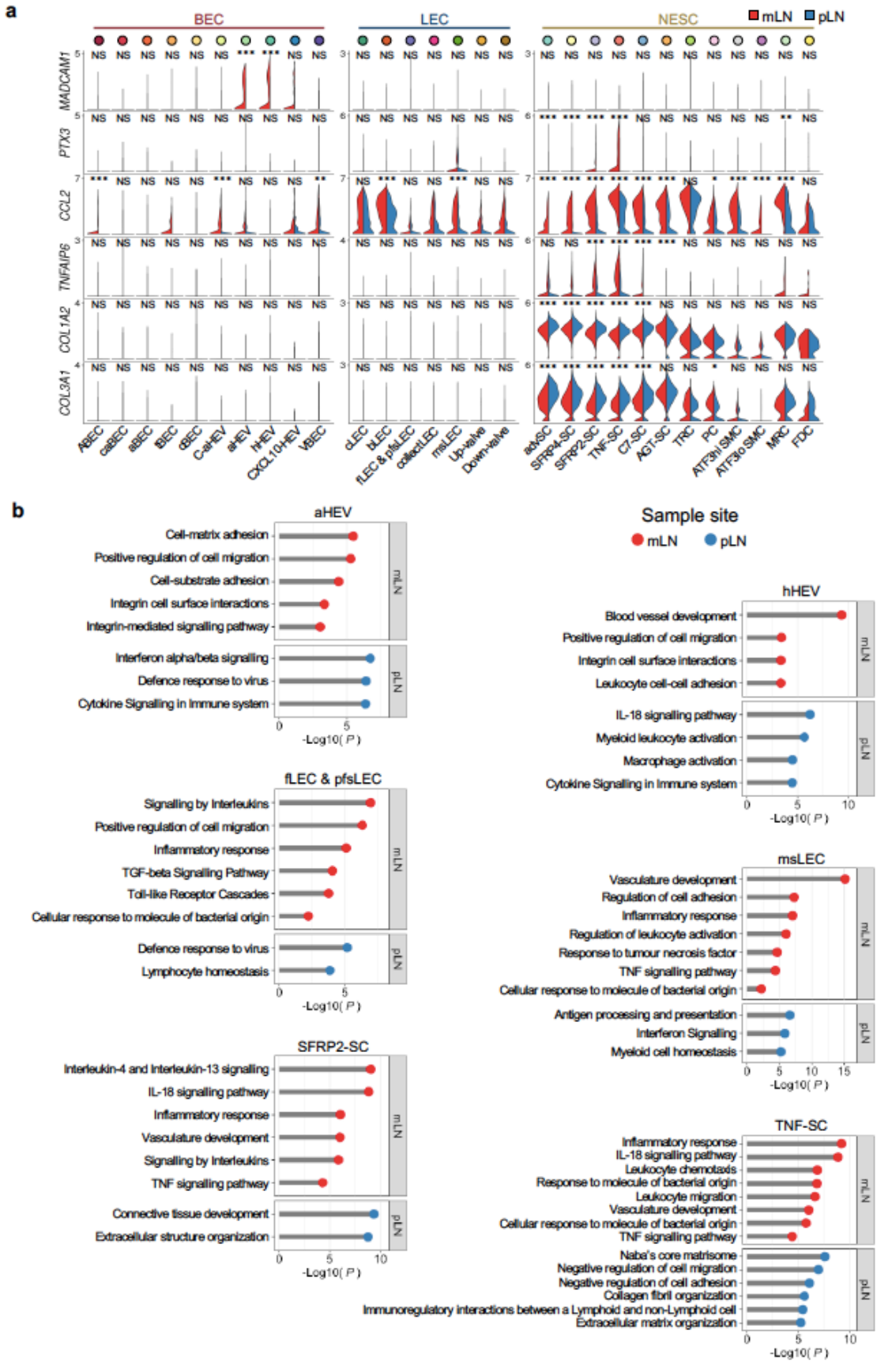
a
BEC
LEC
NESC
mLN
pLN
MADCAM1
PTX3
CCL2
TNFAIP6
COL1A2
COL3A1
ABEC
caBEC
aBEC
tBEC
dBEC
C-aHEV
aHEV
hHEV
CXCL10-HEV
VBEC
cLEC
bLEC
fLEC & pfsLEC
collectLEC
msLEC
Up-valve
Down-valve
adv5C
SFRP4-SC
SFRP2-SC
TNF-SC
C7-SC
AGT-SC
TRC
PC
ATF3hi SMC
ATF3lo SMC
MRC
FDC
b
Sample site
mLN
pLN
aHEV
Cell-matrix adhesion
Positive regulation of cell migration
Cell-substrate adhesion
Integrin cell surface interactions
Integrin-mediated signalling pathway
Interferon alpha/beta signalling
Defence response to virus
Cytokine Signalling in Immune system
-Log10(P)
hHEV
Blood vessel development
Positive regulation of cell migration
Integrin cell surface interactions
Leukocyte cell-cell adhesion
IL-18 signalling pathway
Myeloid leukocyte activation
Macrophage activation
Cytokine Signalling in Immune system
-Log10(P)
fLEC & pfsLEC
Signalling by Interleukins
Positive regulation of cell migration
Inflammatory response
TGF-beta Signalling Pathway
Toll-like Receptor Cascades
Cellular response to molecule of bacterial origin
Defence response to virus
Lymphocyte homeostasis
-Log10(P)
msLEC
Vasculature development
Regulation of cell adhesion
Inflammatory response
Regulation of leukocyte activation
Response to tumour necrosis factor
TNF signalling pathway
Cellular response to molecule of bacterial origin
Antigen processing and presentation
Interferon Signalling
Myeloid cell homeostasis
-Log10(P)
SFRP2-SC
Interleukin-4 and Interleukin-13 signalling
IL-18 signalling pathway
Inflammatory response
Vasculature development
Signalling by Interleukins
TNF signalling pathway
Connective tissue development
Extracellular structure organization
-Log10(P)
TNF-SC
Inflammatory response
IL-18 signalling pathway
Leukocyte chemotaxis
Response to molecule of bacterial origin
Leukocyte migration
Vasculature development
Cellular response to molecule of bacterial origin
TNF signalling pathway
Naba's core matrisome
Negative regulation of cell migration
Negative regulation of cell adhesion
Collagen fibril organization
Immunoregulatory interactions between a Lymphoid and non-Lymphoid cell
Extracellular matrix organization
-Log10(P)

Figure 7.

a, Violin plots comparing expressions of key genes between mLN (red) and pLN (blue) samples according to NHC subclusters. *$P < 0.05$, **$P < 0.01$, ***$P < 0.001$ (two-sided Wilcoxon Rank-Sum test with Bonferroni correction). NS, not significant.

b, Key gene ontologies of DEGs upregulated in mLN (red) or pLN (blue) compared with the other LN type according to representative NHC subclusters.

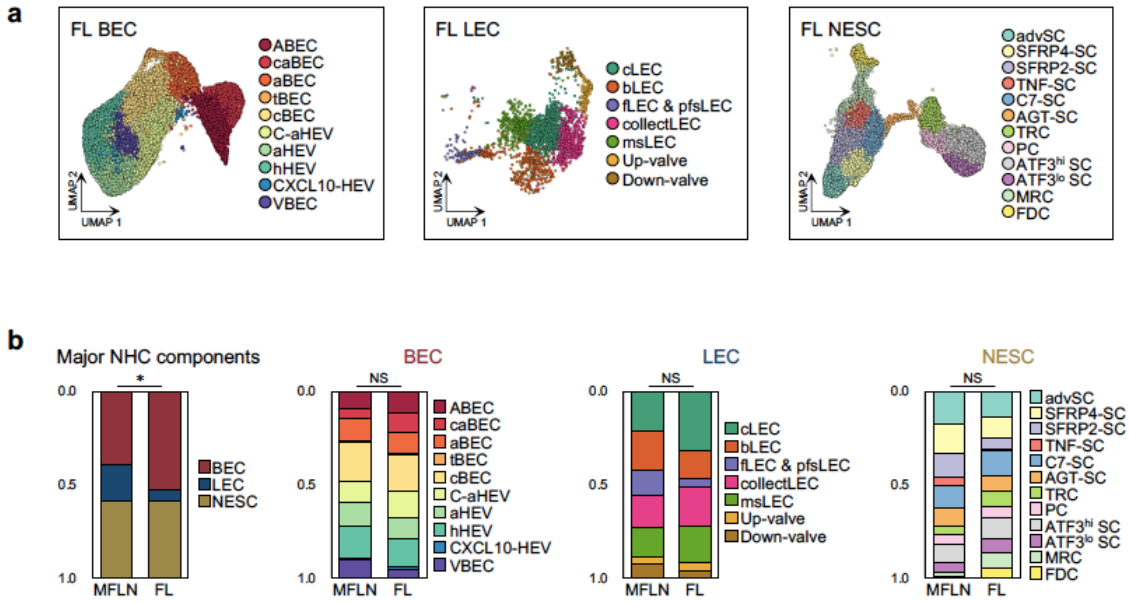

Figure 8.

a, UMAP plots of FL BEC (left), LEC (middle), and NESC (right) subclusters.

b, Differences between MFLN and FL NHC compositions based on major NHC components, BEC, LEC, and NESC subclusters (from left to right). **P* = 0.010 (two-sided chi-squared test). NS, not significant.

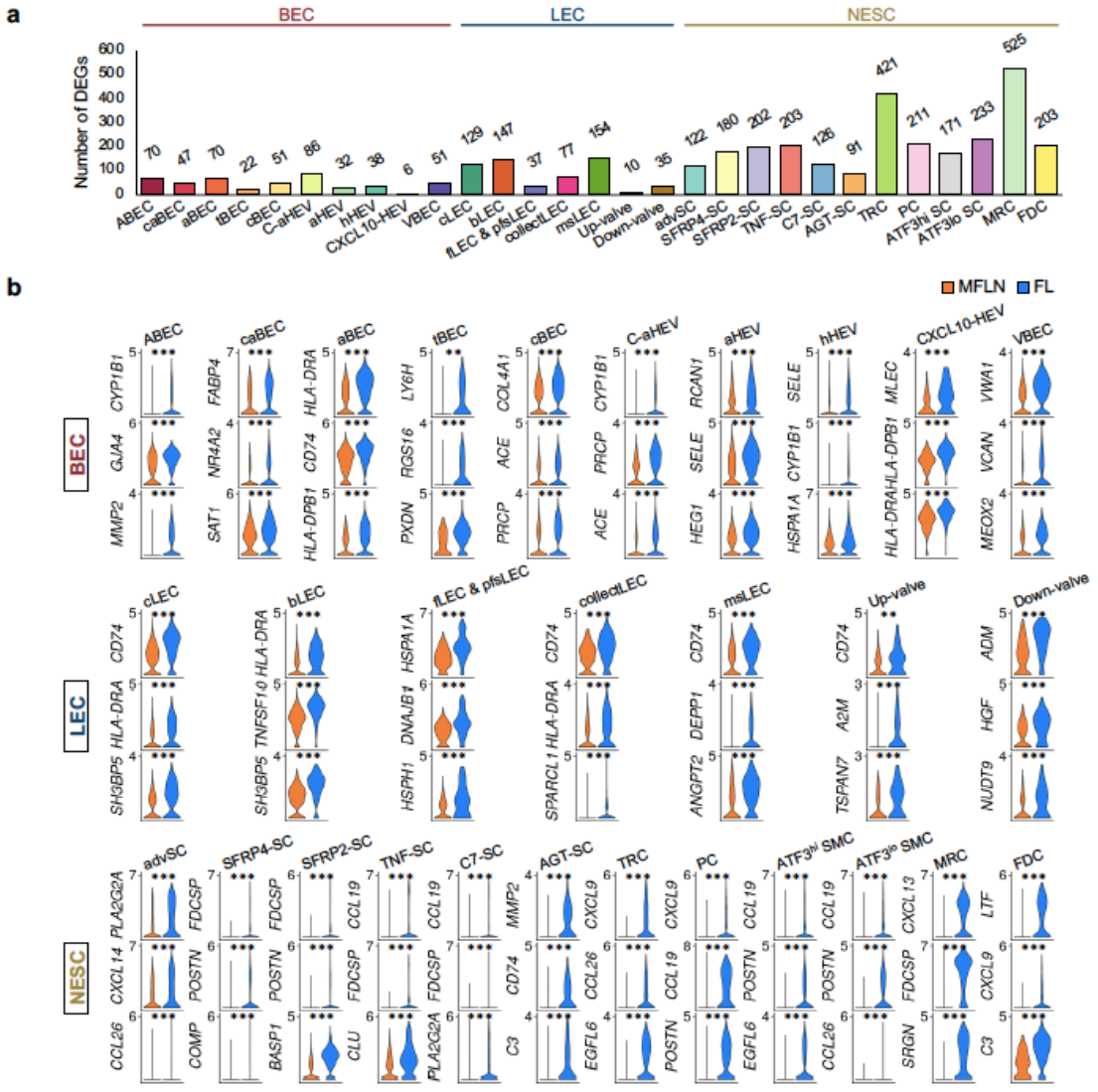
a
BEC
LEC
NESC
Number of DEGs
ABEC
caBEC
aBEC
tBEC
cBEC
C-aHEV
aHEV
hHEV
CXCL10-HEV
VBEC
cLEC
bLEC
fLEC & pfsLEC
collectLEC
msLEC
Up-valve
Down-valve
advSC
SFRP4-SC
SFRP2-SC
TNF-SC
C7-SC
AGT-SC
TRC
PC
ATF3hi SC
ATF3lo SC
MRC
FDC
b
MFLN
FL
BEC
LEC
NESC

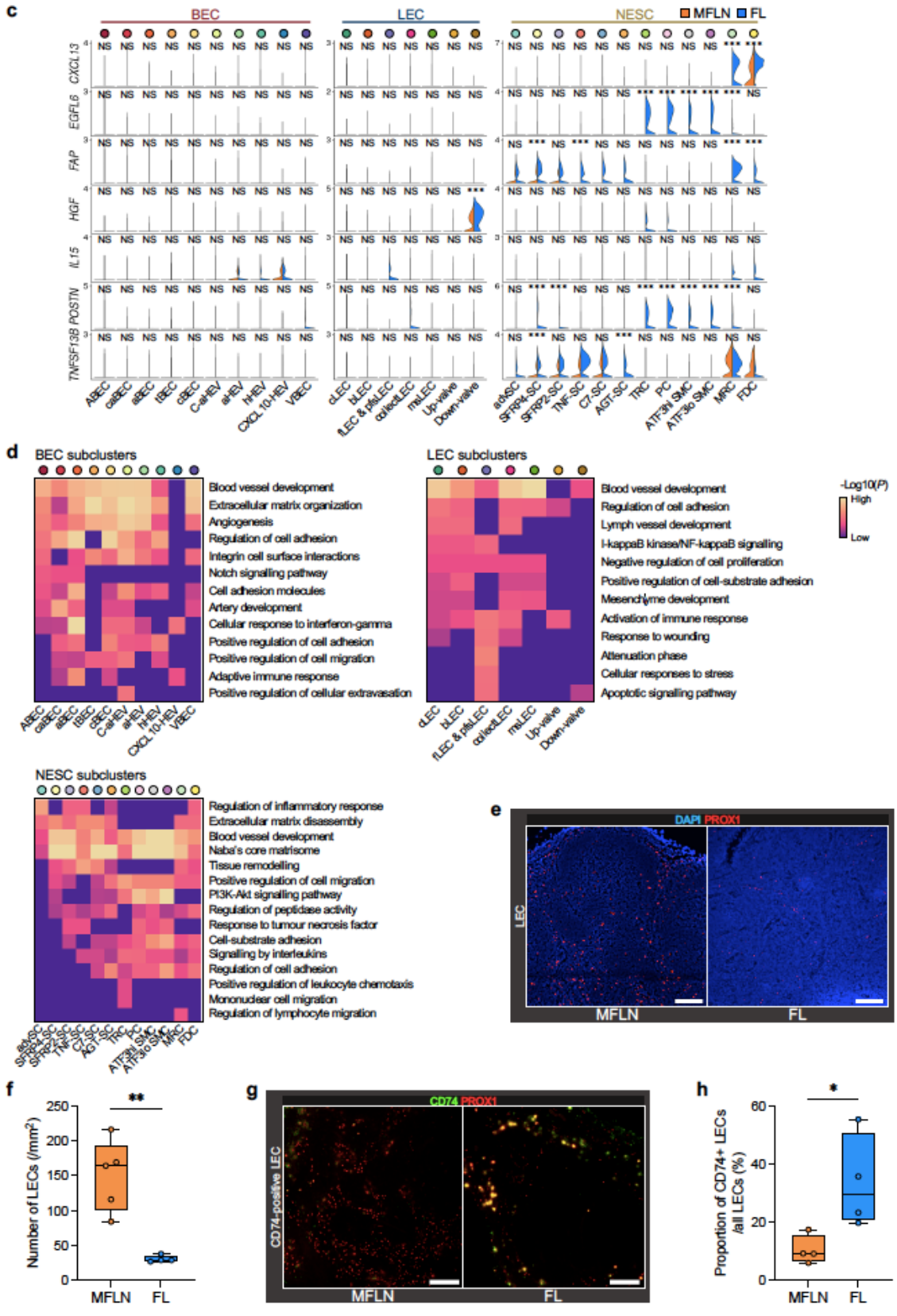
c
BEC
LEC
NESC
MFLN
FL
CXCL13
EGFL6
FAP
HGF
IL15
POSTN
TNFSF13B
d
BEC subclusters
Blood vessel development
Extracellular matrix organization
Angiogenesis
Regulation of cell adhesion
Integrin cell surface interactions
Notch signalling pathway
Cell adhesion molecules
Artery development
Cellular response to interferon-gamma
Positive regulation of cell adhesion
Positive regulation of cell migration
Adaptive immune response
Positive regulation of cellular extravasation
LEC subclusters
Blood vessel development
Regulation of cell adhesion
Lymph vessel development
I-kappaB kinase/NF-kappaB signalling
Negative regulation of cell proliferation
Positive regulation of cell-substrate adhesion
Mesenchyme development
Activation of immune response
Response to wounding
Attenuation phase
Cellular responses to stress
Apoptotic signalling pathway
-Log10(P)
High
Low
NESC subclusters
Regulation of inflammatory response
Extracellular matrix disassembly
Blood vessel development
Naba's core matrisome
Tissue remodelling
Positive regulation of cell migration
PI3K-Akt signalling pathway
Regulation of peptidase activity
Response to tumour necrosis factor
Cell-substrate adhesion
Signalling by interleukins
Regulation of cell adhesion
Positive regulation of leukocyte chemotaxis
Mononuclear cell migration
Regulation of lymphocyte migration
e
DAPI PROX1
LEC
MFLN
FL
f
Number of LECs (/mm²)
MFLN
FL
g
CD74 PROX1
CD74-positive LEC
MFLN
FL
h
Proportion of CD74+ LECs /all LECs (%)
MFLN
FL

Figure 9.

a, Number of DEGs upregulated in FL NHC subclusters compared to MFLN counterparts.

b, Violin plots of top three DEGs upregulated in FL NHC subclusters compared to MFLN counterparts. $^{**}P < 0.01$, $^{***}P < 0.001$ (two-sided Wilcoxon Rank-Sum test with Bonferroni correction).

c, Violin plots comparing expressions of key genes between MFLN (orange) and FL (blue) samples, according to NHC subclusters. $^{***}P < 0.001$ (two-sided Wilcoxon Rank-Sum test with Bonferroni correction). NS, not significant.

d, Gene ontology changes in FL NHC subclusters. GO enrichment analysis of DEGs upregulated in FL BEC (top left), LEC (top right), or NESC (bottom left) subclusters relative to MFLN counterpart subclusters.

e, IF staining of PROX1 (red) showing LEC distribution in representative MFLN (left) and FL (right) samples. Scale bars, 200 μm.

f, Number of PROX1-positive LECs per mm^2, detected by IF staining in biologically independent MFLN ($n = 5$) and FL ($n = 4$) samples. The box plots show the interquartile range (box limits), median (centre line), minimum to max values (whiskers), and samples (circles). $^{**}P = 0.0025$ (two-sided unpaired *t*-test).

g, IF staining of CD74 (green) and PROX1 (red) showing CD74-positive LECs in representative

MFLN (left) and FL (right) samples. Scale bars, 200 μm.

h, Proportions of CD74-positive LECs among PROX1-positive LECs (%) detected by IF staining in biologically independent MFLN ($n = 4$) and FL ($n = 4$) samples. The box plots show the interquartile range (box limits), median (centre line), minimum to max values (whiskers), and samples (circles). *$P = 0.033$ (two-sided unpaired t-test).

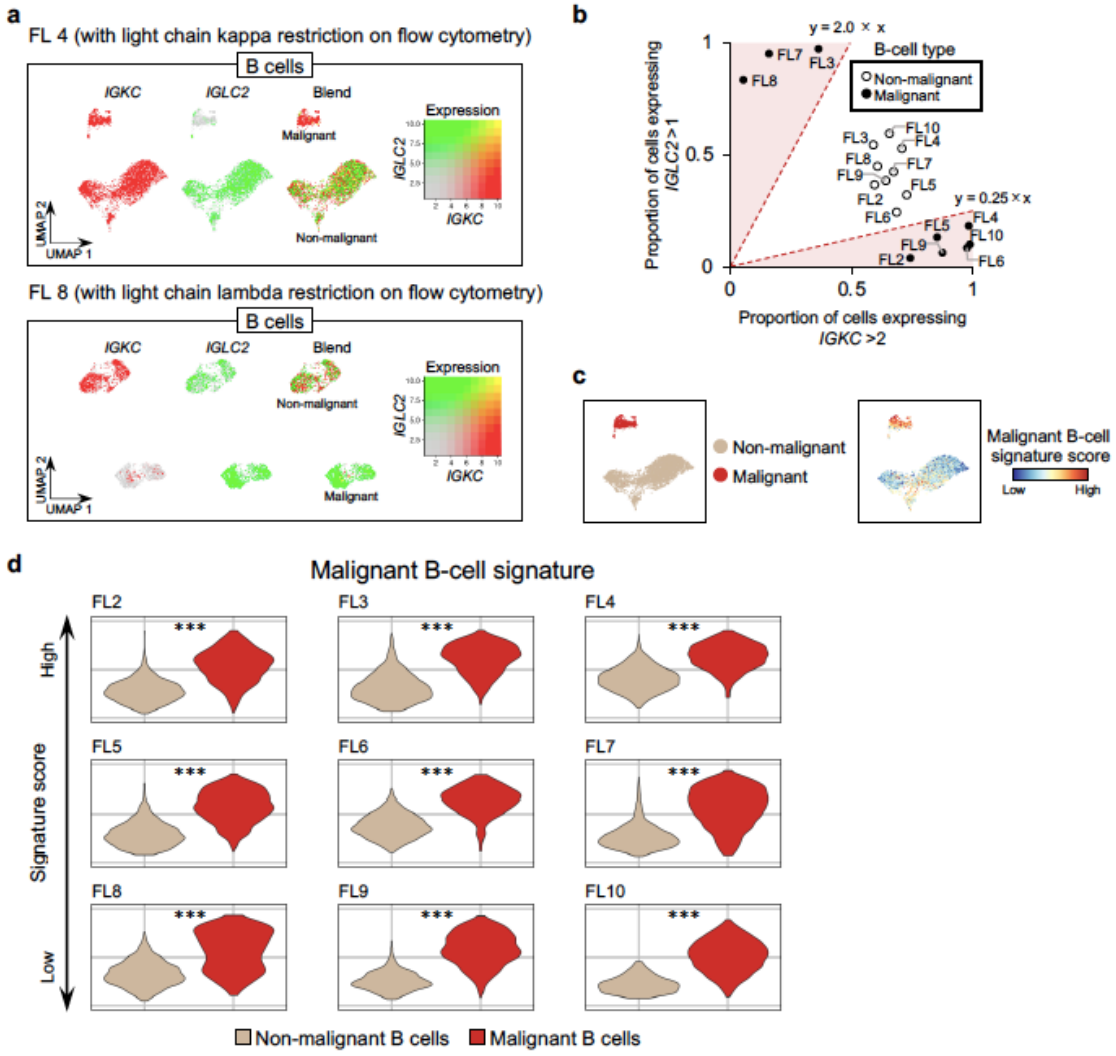

Figure 10.

a, Strategies used to identify malignant B-cell components in FL samples *in silico*. Shown are representative cases with light chain kappa (FL 4; top) or lambda (FL 8; bottom) restrictions confirmed by flow cytometric analysis (data not shown). After identifying B-cell components by detecting *CD79A* expression, I assessed expression of *IGKC* (for light chain kappa) and *IGLC2* (for light chain lambda). Clusters with cells expressing *IGKC* and those expressing

IGLC2 were considered non-malignant B cells, while clusters with cells expressing only one of these genes were considered malignant B cells.

b, Scatter plot showing clear discrimination of malignant (filled circles) from non-malignant (empty circles) B-cell clusters in each FL sample, based on the ratio of cells expressing *IGLC2* (expression level >1; y-axis) to those expressing *IGKC* (expression level >2; x-axis,). Red-shaded areas indicate regions in which the ratio was >2.0 or <0.25.

c, Representative UMAP plots showing B cells from FL 4 according to B-cell types (beige; non-malignant, red; malignant) (left panel) or malignant B-cell signature score (right panel).

d, Violin plots showing malignant B-cell signature score in extracted non-malignant and malignant B cells, according to different FL samples (FL 2–10). ***$P = 1.1 \times 10^{-204}$ (FL 2), ***$P = 0$ (FL 3), ***$P = 3.3 \times 10^{-176}$ (FL 4), ***$P = 0$ (FL 5), ***$P = 4.2 \times 10^{-122}$ (FL 6), ***$P = 0$ (FL 7), ***$P = 4.2 \times 10^{-161}$ (FL 8), ***$P = 3.7 \times 10^{-256}$ (FL 9), ***$P = 2.5 \times 10^{-81}$ (FL 10) (two-sided Wilcoxon Rank-Sum test with Bonferroni correction).

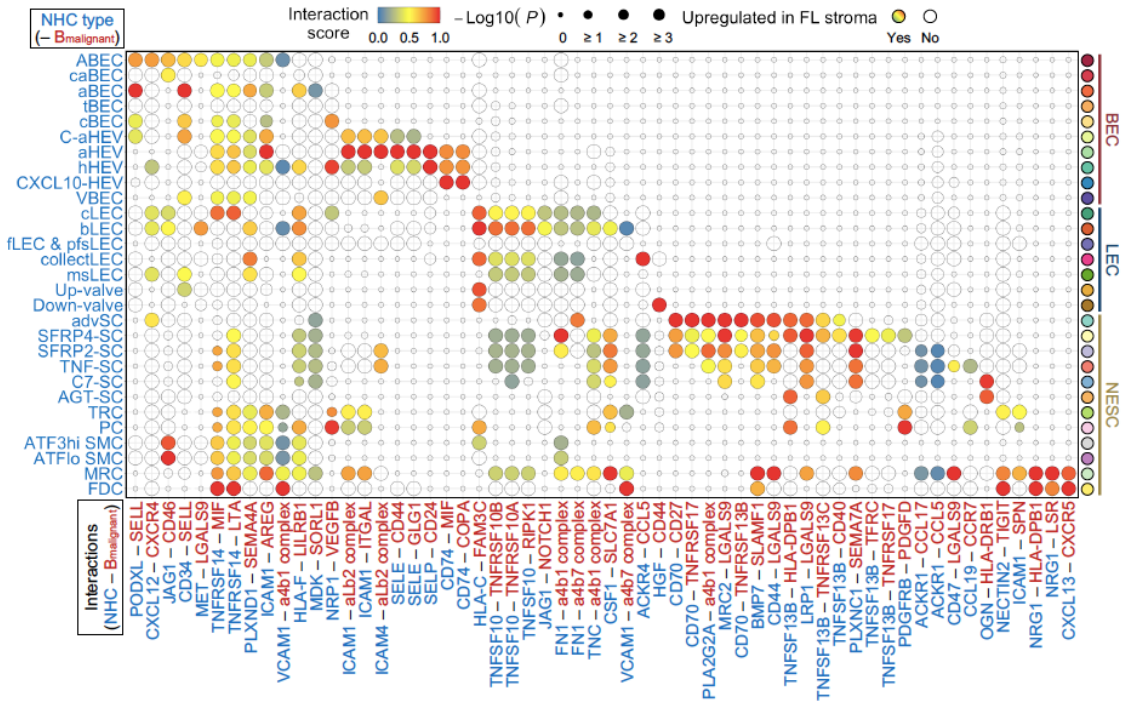

Figure 11.

Enhanced interactions across FL NHC subclusters and malignant B cells ($B_{malignant}$). Circle size indicates the negative log10 of adjusted *P* values (see the Methods section). Circles are coloured when gene expression for the indicated stroma-derived factor is upregulated in relevant FL subclusters compared to that in the MFLN counterparts (log fold-change >0 and adjusted *P* value <0.05).

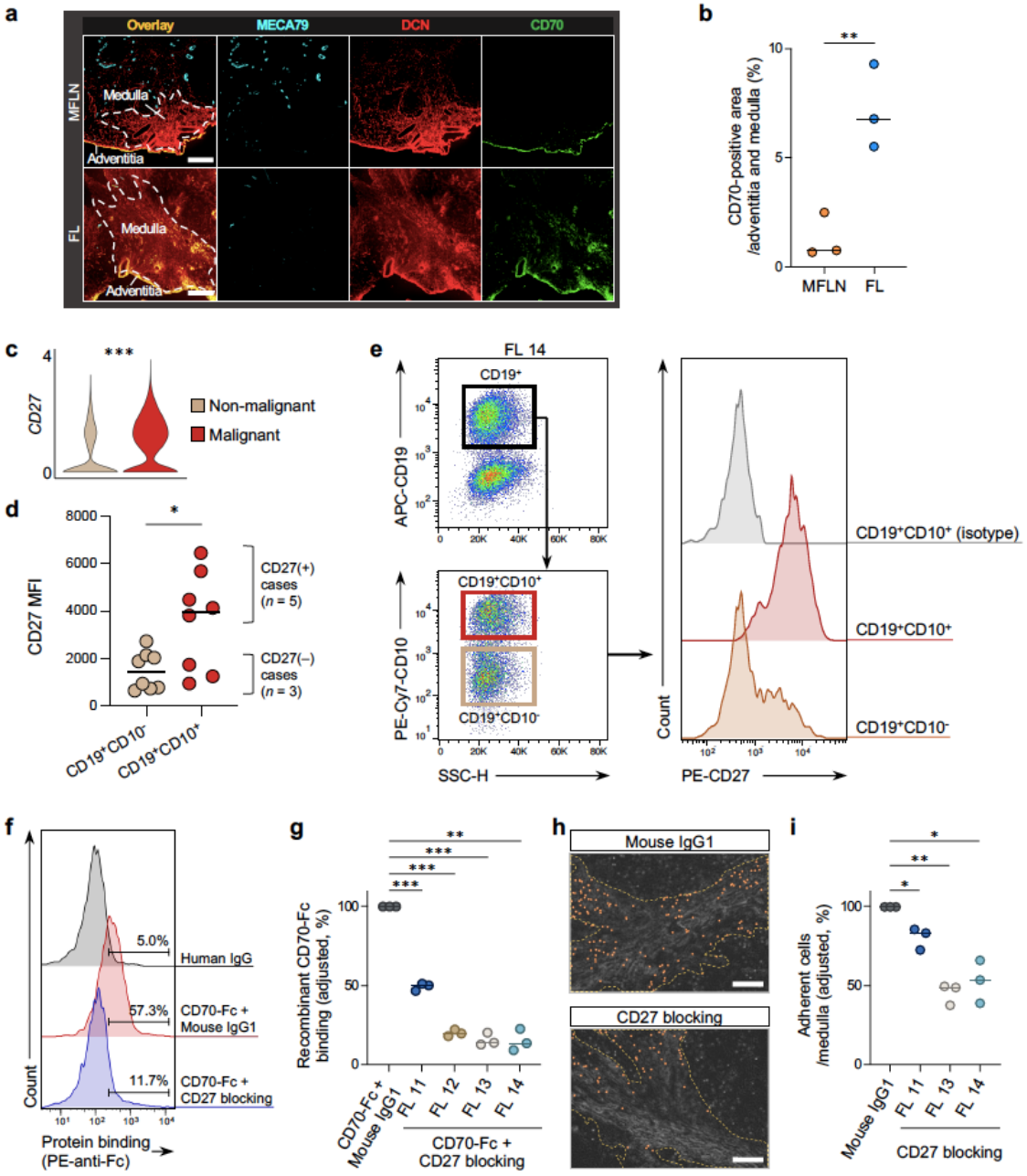

Figure 12.

a, IF staining of MECA-79 (cyan), DCN (red), and CD70 (green) using MFLN (top) and FL (bottom) samples. Scale bars, 200 μm. Representative images from one of three independent experiments are shown.

b, Proportions of CD70-positive area in medullary and adventitia regions of MFLN (n = 3) and FL

(n = 3) samples. Circles represent biologically independent samples. Bars indicate median. **P = 0.0095 (two-sided unpaired t-test).

c, Violin plots showing the expression of *CD27* in non-malignant and malignant B cells. ***P = 0 (two-sided Wilcoxon Rank-Sum test with Bonferroni correction).

d, Comparison of CD27 mean fluorescence intensity (MFI) between FL $CD19^+CD10^-$ (non-malignant B-cell fraction) and $CD19^+CD10^+$ (malignant B-cell fraction) cells. Circles represent biologically independent samples (n = 8; FL 11–18). *P = 0.039 (two-sided Wilcoxon matched-pairs signed rank test).

e, Flow cytometric analysis of CD27 expression on $CD19^+CD10^-$ and $CD19^+CD10^+$ cells of a representative FL sample (FL 14).

f, Binding of FL $CD19^+CD10^+$ cells to CD70-Fc protein with an anti-CD27 blocking antibody or isotype human IgG. The histograms represent three independent experiments (FL 13).

g, Blocking of FL $CD19^+CD10^+$ cell binding to CD70-Fc protein after treating cells with an anti-CD27 blocking antibody (n = 3) or isotype mouse IgG1 (n = 3) in CD27-positive FL cases (FL 11–14). Proportions of cells bound to CD70-Fc protein were adjusted by subtracting non-specific binding observed with human IgG. CD70-Fc protein binding to cells treated with isotype mouse IgG1 was set to 100% in each experiment. Circles represent independent

experiments. Bars indicate median. $^{**}P = 0.0022$, $^{***}P = 7.3 \times 10^{-4}$ (FL 11), $^{***}P = 2.2 \times 10^{-4}$ (FL 12), $^{***}P = 7.6 \times 10^{-4}$ (FL 13) (two-sided paired *t*-test).

h, Representative malignant B-enriched cell (FL14) adhesion to medullary regions of FL in the presence of an isotype mouse IgG1 (top) or anti-CD27 antibody (bottom). Orange dots indicate adherent cells. Yellow dashed lines indicate medullary regions. Scale bars, 200 μm.

i, Blocking of malignant B-enriched cell (FL 11,13,14) adhesion to FL medullary regions (per mm^2) after treating cells with an anti-CD27 blocking antibody ($n = 3$) or isotype mouse IgG1 ($n = 3$). Adhesion of cells treated with isotype mouse IgG1 was set to 100% in each experiment. Circles represent independent experiments. Bars indicate median. $^{*}P = 0.041$ (FL 11), $^{*}P = 0.027$ (FL 14), $^{**}P = 0.0050$ (two-sided paired *t*-test).

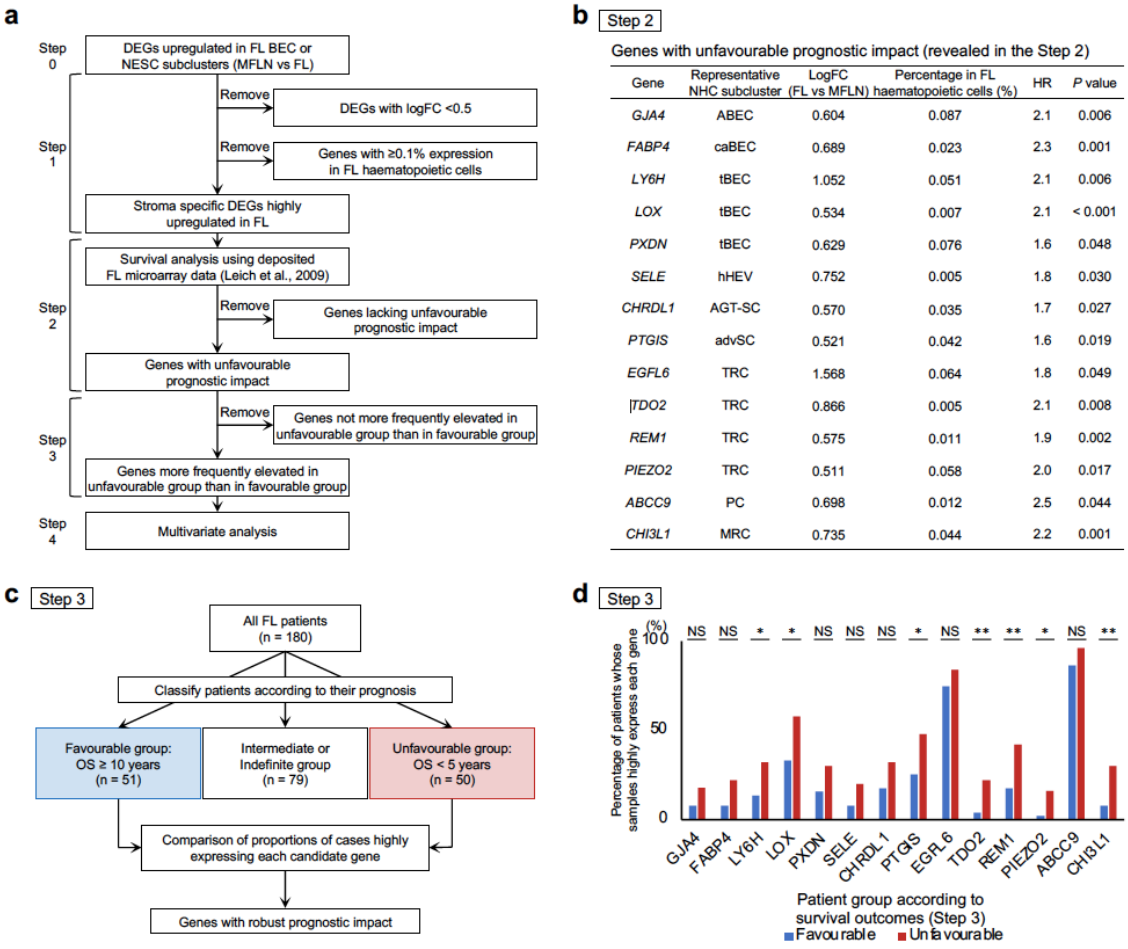

Figure 13.

a, Scheme of stepwise survival analysis using public data from FL patients[48] to identify stroma-derived prognostic markers.

b, Genes with unfavourable prognostic impact, as revealed by survival analysis using Kaplan–Meier methods with the two-sided log-rank test (Step 2). Representative NHC subcluster denotes subclusters in which indicated gene expression is most greatly upregulated. FC, fold-change; HR, hazard ratio.

c, Strategies used to confirm prognostic impact of candidate genes identified in Step 2 (Step 3).

OS, overall survival.

d, Results of analysis performed in Step 3. Shown is the proportion of patients whose samples highly expressed indicated genes in favourable or unfavourable prognostic groups. **P* = 0.034 (*LY6H*), **P* = 0.017 (*LOX*), **P* = 0.024 (*PTGIS*), **P* = 0.014 (*PIEZO2*), **P* = 0.027 (*CHI3L1*), ***P* = 0.0077 (*TDO2*), ***P* = 0.0092 (*REM1*) (two-sided Fisher's exact test). NS, not significant.

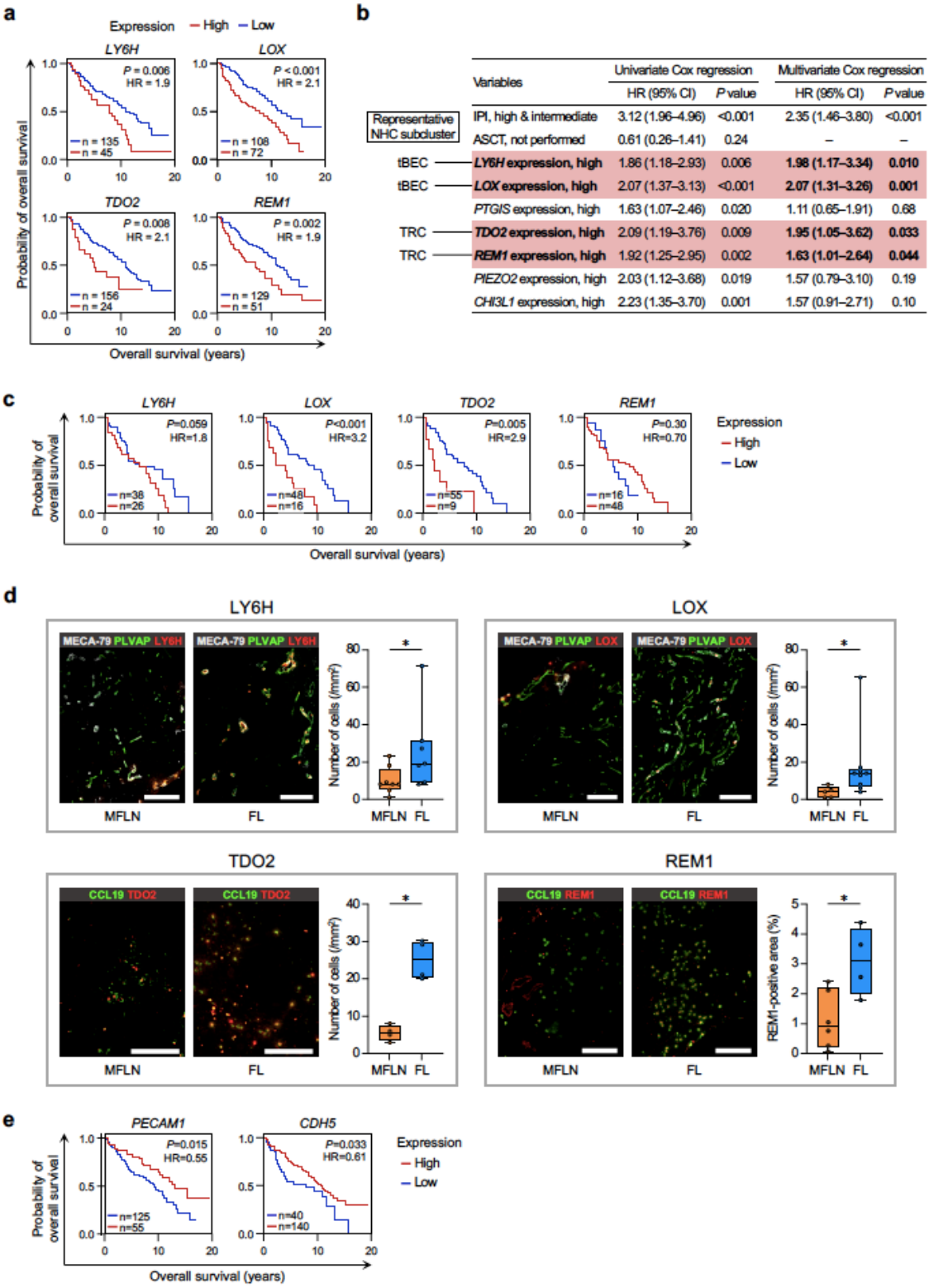

Figure 14.

a, Kaplan–Meier curves showing overall survival of newly diagnosed FL patients (n = 180) based

on expression of *LY6H* (top left), *LOX* (top right), *TDO2* (bottom left), and *REM1* (bottom right). Statistical analysis was performed using the two-sided log-rank test. HR, hazard ratio.

b, Univariate and multivariate Cox regression analysis predicting overall survival (n = 180). Statistical analysis was performed using the two-sided Cox proportional-hazards analysis. Significant gene expression in multivariate analysis is indicated using red-highlighted text. Representative NHC subcluster denotes subclusters in which indicated gene expression is most greatly upregulated in FL. CI, confidence interval.

c, Estimation of overall survival based on expression of *LY6H*, *LOX*, *TDO2*, and *REM1* in the FL patients of the intermediate prognosis group (n = 64, two-sided log-rank test).

d, IF staining of LY6H (red, top left), LOX (red, top right), TDO2 (red, bottom left), and REM1 (red, bottom right) in representative MFLN and FL samples (left and right panels, respectively). Scale bars, 200 μm. The box plots show the interquartile range (box limits), median (centre line), minimum to max values (whiskers), and biologically independent samples (circles) for quantification of cell number (for LY6H, LOX, and TDO2) or area (for REM1) positive for each protein in MFLN and FL samples (MFLN, n = 8, 5, 4, and 6; FL, n = 7, 9, 4, and 4 for LY6H, LOX, TDO2, and REM1, respectively). *P = 0.029 (LY6H), *P = 0.010 (LOX), *P = 0.029 (TDO2), *P = 0.038 (REM1) (two-sided Mann–Whitney U-test).

e, Estimation of overall survival based on expression of *PECAM1* and *CDH5*.

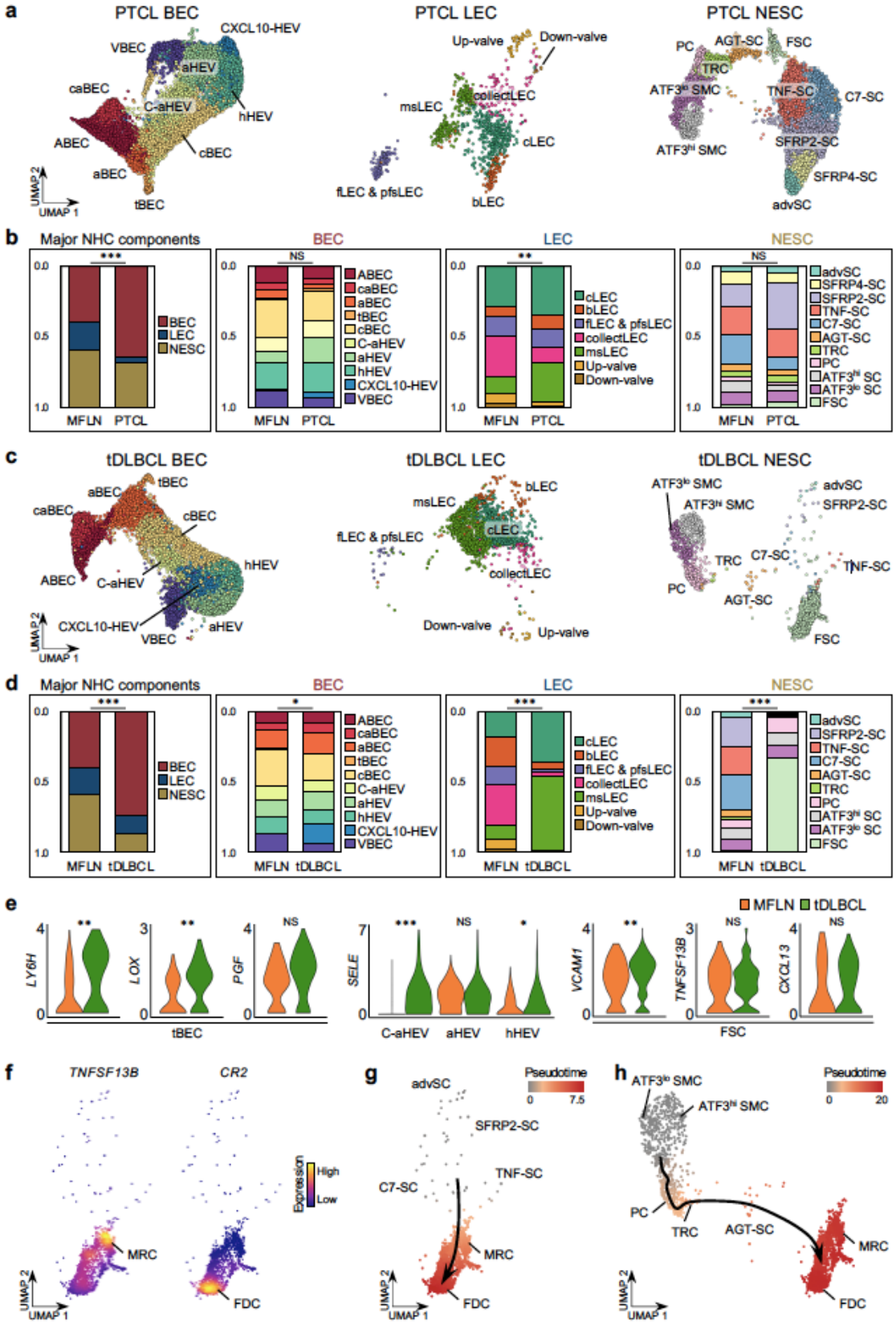
a
PTCL BEC
CXCL10-HEV
VBEC
aHEV
caBEC
C-aHEV
hHEV
ABEC
cBEC
aBEC
tBEC
UMAP 2
UMAP 1
PTCL LEC
Up-valve
Down-valve
msLEC
collectLEC
cLEC
fLEC & pfsLEC
bLEC
PTCL NESC
PC
AGT-SC
FSC
TRC
ATF3hi SMC
TNF-SC
C7-SC
ATF3lo SMC
SFRP2-SC
SFRP4-SC
advSC
b
Major NHC components
BEC
LEC
NESC
MFLN
PTCL
ABEC
caBEC
aBEC
tBEC
cBEC
C-aHEV
aHEV
hHEV
CXCL10-HEV
VBEC
cLEC
bLEC
fLEC & pfsLEC
collectLEC
msLEC
Up-valve
Down-valve
advSC
SFRP4-SC
SFRP2-SC
TNF-SC
C7-SC
AGT-SC
TRC
PC
ATF3hi SC
ATF3lo SC
FSC
c
tDLBCL BEC
tDLBCL LEC
tDLBCL NESC
d
tDLBCL
e
MFLN
tDLBCL
LY6H
LOX
PGF
SELE
VCAM1
TNFSF13B
CXCL13
tBEC
C-aHEV
aHEV
hHEV
FSC
f
TNFSF13B
CR2
High
Low
Expression
MRC
FDC
g
Pseudotime
h

Figure 15.

a, UMAP plots of PTCL BEC (left), LEC (middle), and NESC (right) subclusters.

b, Compositional differences between PTCL and MFLN NHCs based on major NHC components, BEC subclusters, LEC subclusters, and NESC subclusters (from left to right). $^{**}P = 0.0076$, $^{***}P = 2.7 \times 10^{-4}$ (two-sided chi-squared test). NS, not significant.

c, UMAP plots of tDLBCL BEC (left), LEC (middle), and NESC (right) subclusters.

d, Compositional differences between tDLBCL and MFLN NHCs based on major NHC components, BEC subclusters, LEC subclusters, and NESC subclusters (from left to right). $^{*}P = 0.030$, $^{***}P = 3.4 \times 10^{-6}$ (Major NHC components), $^{***}P = 6.3 \times 10^{-16}$ (LEC), $^{***}P = 1.1 \times 10^{-23}$ (NESC) (two-sided chi-squared test).

e, Violin plots comparing expressions of key genes between MFLN (orange) and tDLBCL (green) samples according to selected NHC subclusters. $^{*}P = 0.015$, $^{**}P = 0.0039$ (*LY6H*), $^{**}P = 0.0090$ (*LOX*), $^{**}P = 0.0075$ (*VCAM1*), $^{***}P = 8.0 \times 10^{-111}$ (two-sided Wilcoxon Rank-Sum test with Bonferroni correction). NS, not significant.

f, Expression of *TNFSF13B* (left) and *CR2* (right) in tDLBCL follicular stromal cells identifying MRCs and FDCs, respectively.

g,h, Pseudo-time developmental stages in tDLBCL advSCs, SFRP2-SCs, TNF-SCs, C7-SCs, MRCs, and FDCs (**g**) or in tDLBCL SMC subclusters, PCs, TRCs, AGT-SCs, MRCs, and FDCs

(**h**). Dark winding lines in the cell objects indicate putative developmental trajectories.

8. Tables

Table 1.
Previous reports regarding LNNHC heterogeneity analyzed by scRNA-seq.

Species	**LN status**	**BEC**	**LEC**	**NESC**
Human	Normal LN	**yet**	Takeda et al.[23]	**yet**
	Disease	**yet**	**yet**	**yet**
Mouse	Normal LN	Brulois et al.[26]	Xiang et al.[24]	Rodda et al.[22]
	Disease	Brulois et al.[26] (inflammation)	Xiang et al.[24] (inflammation)	Rodda et al.[22] (inflammation)

Table 2.

Characteristics of patients in the MFLN (top) and FL (middle) cohorts and comparison of patient cohorts (bottom).

Representative somatic mutations of FL (reference 11) are listed.

Statistical analysis was performed using the two-sided Mann–Whitney *U*-test and two-sided Fisher's exact test for age and sex comparison, respectively.

F, female; IQR, interquartile range; M, male; NA, not available; ND, newly diagnosed; R, relapsed.

MFLN cohort

No.	Age	Sex	Disease	Sample site	Number of analysed NHCs
1	66	M	Sigmoid colon and rectal cancer	Mesenteric	6,152
2	70	M	Rectal cancer	Mesenteric	4,014
3	59	F	Sigmoid colon cancer	Mesenteric	11,815
4	72	M	Sigmoid colon cancer	Mesenteric	9,552
5	50	F	Descending colon cancer	Mesenteric	5,328
6	75	F	Descending colon cancer	Mesenteric	10,995
7	39	F	Breast cancer	Axillary	8,366
8	39	F	Thyroid follicular tumor	Cervical	7,371
9	76	F	Breast cancer	Axillary	4,718

FL cohort

No.	Age	Sex	ND or R	Grade	Recurrent somatic mutations of FL	Sample site	Number of analysed NHCs
1	54	F	R	2	NA	Intraperitoneal	1,264
2	70	M	R	2	*KMT2D*, *BCL2*, *EZH2*	Axillary	6,555
3	72	M	ND	2	*CREBBP*, *STAT6*, *KMT2D*, *TNFRSF14*	Submandibular	3,347
4	54	F	ND	2	*CREBBP*	Cervical	9,311
5	48	M	ND	2	–	Cervical	6,220

6	56	F	R	1	*CREBBP*	Cervical	11,364
7	39	F	ND	1	*CREBBP*, *STAT6*, *KMT2D, HIST1H1D*	Cervical	5,060
8	72	M	ND	2	*CREBBP*, *STAT6*, *BCL2*, *EZH2*	Cervical	8,086
9	71	M	ND	3a	*CREBBP*, *STAT6*, *BCL2, TNFRSF14, HIST1H1D*	Inguinal	7,035
10	62	F	R	2	*CREBBP*, *KMT2D*	Cervical	8,679

Cohort comparison

Factors	Cohort		*P* value
	MFLN (n = 9)	FL (n = 10)	
Age, years [median (IQR)]	66 (50, 72)	59 (54, 70)	0.71
Sex, female (%)	6 (66.7)	5 (50.0)	0.65

Table 3.

Clinical characteristics of patients in PTCL (top) and tDLBCL (bottom) cohorts.
F, female; M, male; ND, newly diagnosed; R, relapsed.

PTCL cohort

No.	Age	Sex	ND or R	PTCL subtype	Sample site
1	71	M	ND	ALK-positive anaplastic large cell lymphoma	Cervical
2	77	M	ND	Follicular T-cell lymphoma	Cervical
3	78	F	ND	Peripheral T-cell lymphoma, not otherwise specified	Cervical
4	79	M	ND	Angioimmunoblastic T-cell lymphoma (+ myelodysplastic syndrome)	Cervical
5	87	M	ND	Peripheral T-cell lymphoma, not otherwise specified	Cervical

tDLBCL cohort

No.	Age	Sex	ND or R	Sample site
1	67	M	ND	Intraperitoneal
2	74	F	R	Cervical
3	83	F	R	Cervical

9. Acknowledgments

Throughout the PhD program, I received great support and assistance.

First, I would like to thank Professor Shigeru Chiba and Professor Mamiko Sakata-Yanagimoto for directing and supervising the entire research project, teaching me a lot of invaluable knowledge in science research, and supporting my experiments, data analysis, and writing a manuscript.

I also thank all support from the Hematology Laboratory members, which made my research possible. I would like to thank all co-authors for providing human samples and helping me for immunostaining experiments.

I thank the staffs at associated institutions and departments for cooperation in human sample collection, Eiko Matsuzawa and Yukari Sakashita for technical assistance, and Ayako Suzuki and Yutaka Suzuki (the University of Tokyo) for supporting computational analysis of scRNA-seq data.

The contents published in Nature Cell Biology (2022 Mar 24. doi: 10.1038/s41556-022-00866-3. Online ahead of print) are re-used in this dissertation following based on the approval from Springer Nature (https://www.nature.com/nature-portfolio/reprints-and-permissions/permissions-requests).

10. References

1. Swerdlow, S.*, et al.* WHO Classification of Tumours of Haematopoietic & Lymphoid Tissues, 4th ed., Revised ed: International Agency for Research on Cancer; 2017.

2. Scott, D.W. & Gascoyne, R.D. The tumour microenvironment in B cell lymphomas. *Nature reviews. Cancer* **14**, 517-534 (2014).

3. Höpken, U.E. & Rehm, A. Targeting the Tumor Microenvironment of Leukemia and Lymphoma. *Trends in cancer* **5**, 351-364 (2019).

4. De Palma, M., Biziato, D. & Petrova, T.V. Microenvironmental regulation of tumour angiogenesis. *Nature reviews. Cancer* **17**, 457-474 (2017).

5. Sahai, E.*, et al.* A framework for advancing our understanding of cancer-associated fibroblasts. *Nature reviews. Cancer* **20**, 174-186 (2020).

6. Ruan, J., Hajjar, K., Rafii, S. & Leonard, J.P. Angiogenesis and antiangiogenic therapy in non-Hodgkin's lymphoma. *Annals of oncology : official journal of the European Society for Medical Oncology* **20**, 413-424 (2009).

7. Lenz, G.*, et al.* Stromal gene signatures in large-B-cell lymphomas. *The New England journal of medicine* **359**, 2313-2323 (2008).

8. Medina, D.J.*, et al.* Mesenchymal stromal cells protect mantle cell lymphoma cells from spontaneous and drug-induced apoptosis through secretion of B-cell activating factor and

activation of the canonical and non-canonical nuclear factor κB pathways. *Haematologica* **97**, 1255-1263 (2012).

9. Mourcin, F., Pangault, C., Amin-Ali, R., Amé-Thomas, P. & Tarte, K. Stromal cell contribution to human follicular lymphoma pathogenesis. *Frontiers in immunology* **3**, 280 (2012).

10. Valkenburg, K.C., de Groot, A.E. & Pienta, K.J. Targeting the tumour stroma to improve cancer therapy. *Nature reviews. Clinical oncology* **15**, 366-381 (2018).

11. Carbone, A.*, et al.* Follicular lymphoma. *Nature reviews. Disease primers* **5**, 83 (2019).

12. Guilloton, F.*, et al.* Mesenchymal stromal cells orchestrate follicular lymphoma cell niche through the CCL2-dependent recruitment and polarization of monocytes. *Blood* **119**, 2556-2567 (2012).

13. Horning, S.J. & Rosenberg, S.A. The natural history of initially untreated low-grade non-Hodgkin's lymphomas. *The New England journal of medicine* **311**, 1471-1475 (1984).

14. Husson, H.*, et al.* CXCL13 (BCA-1) is produced by follicular lymphoma cells: role in the accumulation of malignant B cells. *British journal of haematology* **119**, 492-495 (2002).

15. Tjin, E.P.*, et al.* Functional analysis of HGF/MET signaling and aberrant HGF-activator expression in diffuse large B-cell lymphoma. *Blood* **107**, 760-768 (2006).

16. Lwin, T.*, et al.* Lymphoma cell adhesion-induced expression of B cell-activating factor of the

TNF family in bone marrow stromal cells protects non-Hodgkin's B lymphoma cells from apoptosis. *Leukemia* **23**, 170-177 (2009).

17. Epron, G.*, et al.* Monocytes and T cells cooperate to favor normal and follicular lymphoma B-cell growth: role of IL-15 and CD40L signaling. *Leukemia* **26**, 139-148 (2012).

18. Link, A.*, et al.* Fibroblastic reticular cells in lymph nodes regulate the homeostasis of naive T cells. *Nature immunology* **8**, 1255-1265 (2007).

19. Krishnamurty, A.T. & Turley, S.J. Lymph node stromal cells: cartographers of the immune system. *Nature immunology* **21**, 369-380 (2020).

20. Chang, J.E. & Turley, S.J. Stromal infrastructure of the lymph node and coordination of immunity. *Trends in immunology* **36**, 30-39 (2015).

21. Fletcher, A.L., Acton, S.E. & Knoblich, K. Lymph node fibroblastic reticular cells in health and disease. *Nature reviews. Immunology* **15**, 350-361 (2015).

22. Rodda, L.B.*, et al.* Single-Cell RNA Sequencing of Lymph Node Stromal Cells Reveals Niche-Associated Heterogeneity. *Immunity* **48**, 1014-1028.e1016 (2018).

23. Takeda, A.*, et al.* Single-Cell Survey of Human Lymphatics Unveils Marked Endothelial Cell Heterogeneity and Mechanisms of Homing for Neutrophils. *Immunity* **51**, 561-572.e565 (2019).

24. Xiang, M.*, et al.* A Single-Cell Transcriptional Roadmap of the Mouse and Human Lymph

Node Lymphatic Vasculature. *Frontiers in cardiovascular medicine* **7**, 52 (2020).

25. Fujimoto, N.*, et al.* Single-cell mapping reveals new markers and functions of lymphatic endothelial cells in lymph nodes. *PLoS biology* **18**, e3000704 (2020).

26. Brulois, K.*, et al.* A molecular map of murine lymph node blood vascular endothelium at single cell resolution. *Nature communications* **11**, 3798 (2020).

27. Kapoor, V.N.*, et al.* Gremlin 1(+) fibroblastic niche maintains dendritic cell homeostasis in lymphoid tissues. *Nature immunology* **22**, 571-585 (2021).

28. Zhao, Q.*, et al.* Single-Cell Transcriptome Analyses Reveal Endothelial Cell Heterogeneity in Tumors and Changes following Antiangiogenic Treatment. *Cancer research* **78**, 2370-2382 (2018).

29. Baryawno, N.*, et al.* A Cellular Taxonomy of the Bone Marrow Stroma in Homeostasis and Leukemia. *Cell* **177**, 1915-1932.e1916 (2019).

30. Yang, S.*, et al.* Decontamination of ambient RNA in single-cell RNA-seq with DecontX. *Genome biology* **21**, 57 (2020).

31. Young, M.D. & Behjati, S. SoupX removes ambient RNA contamination from droplet-based single-cell RNA sequencing data. *GigaScience* **9**(2020).

32. Butler, A., Hoffman, P., Smibert, P., Papalexi, E. & Satija, R. Integrating single-cell transcriptomic data across different conditions, technologies, and species. *Nature*

biotechnology **36**, 411-420 (2018).

33. Fang, J.S.*, et al.* Shear-induced Notch-Cx37-p27 axis arrests endothelial cell cycle to enable arterial specification. *Nature communications* **8**, 2149 (2017).

34. Fleming, R.E.*, et al.* Carbonic anhydrase IV expression in rat and human gastrointestinal tract regional, cellular, and subcellular localization. *The Journal of clinical investigation* **96**, 2907-2913 (1995).

35. Thiriot, A.*, et al.* Differential DARC/ACKR1 expression distinguishes venular from non-venular endothelial cells in murine tissues. *BMC biology* **15**, 45 (2017).

36. Kalucka, J.*, et al.* Single-Cell Transcriptome Atlas of Murine Endothelial Cells. *Cell* **180**, 764-779.e720 (2020).

37. Finak, G.*, et al.* MAST: a flexible statistical framework for assessing transcriptional changes and characterizing heterogeneity in single-cell RNA sequencing data. *Genome biology* **16**, 278 (2015).

38. Streeter, P.R., Berg, E.L., Rouse, B.T., Bargatze, R.F. & Butcher, E.C. A tissue-specific endothelial cell molecule involved in lymphocyte homing. *Nature* **331**, 41-46 (1988).

39. Berlin, C.*, et al.* Alpha 4 beta 7 integrin mediates lymphocyte binding to the mucosal vascular addressin MAdCAM-1. *Cell* **74**, 185-195 (1993).

40. von Andrian, U.H. & Mempel, T.R. Homing and cellular traffic in lymph nodes. *Nature*

reviews. Immunology **3**, 867-878 (2003).

41. Lee, M.*, et al.* Transcriptional programs of lymphoid tissue capillary and high endothelium reveal control mechanisms for lymphocyte homing. *Nature immunology* **15**, 982-995 (2014).

42. Zhou, Y.*, et al.* Metascape provides a biologist-oriented resource for the analysis of systems-level datasets. *Nature communications* **10**, 1523 (2019).

43. Trapnell, C.*, et al.* The dynamics and regulators of cell fate decisions are revealed by pseudotemporal ordering of single cells. *Nature biotechnology* **32**, 381-386 (2014).

44. Andor, N.*, et al.* Single-cell RNA-Seq of follicular lymphoma reveals malignant B-cell types and coexpression of T-cell immune checkpoints. *Blood* **133**, 1119-1129 (2019).

45. Roider, T.*, et al.* Dissecting intratumour heterogeneity of nodal B-cell lymphomas at the transcriptional, genetic and drug-response levels. *Nature cell biology* **22**, 896-906 (2020).

46. Hänzelmann, S., Castelo, R. & Guinney, J. GSVA: gene set variation analysis for microarray and RNA-seq data. *BMC bioinformatics* **14**, 7 (2013).

47. Vento-Tormo, R.*, et al.* Single-cell reconstruction of the early maternal-fetal interface in humans. *Nature* **563**, 347-353 (2018).

48. Leich, E.*, et al.* Follicular lymphomas with and without translocation t(14;18) differ in gene expression profiles and genetic alterations. *Blood* **114**, 826-834 (2009).

49. Hothorn, T. & Zeileis, A. Generalized maximally selected statistics. *Biometrics* **64**, 1263-1269

(2008).

50. Lambrechts, D.*, et al.* Phenotype molding of stromal cells in the lung tumor microenvironment. *Nature medicine* **24**, 1277-1289 (2018).

51. Goveia, J.*, et al.* An Integrated Gene Expression Landscape Profiling Approach to Identify Lung Tumor Endothelial Cell Heterogeneity and Angiogenic Candidates. *Cancer cell* **37**, 21-36.e13 (2020).

52. Bondareva, O.*, et al.* Identification of atheroprone shear stress responsive regulatory elements in endothelial cells. *Cardiovascular research* **115**, 1487-1499 (2019).

53. Heckmann, B.L., Zhang, X., Xie, X. & Liu, J. The G0/G1 switch gene 2 (G0S2): regulating metabolism and beyond. *Biochimica et biophysica acta* **1831**, 276-281 (2013).

54. Veerman, K., Tardiveau, C., Martins, F., Coudert, J. & Girard, J.P. Single-Cell Analysis Reveals Heterogeneity of High Endothelial Venules and Different Regulation of Genes Controlling Lymphocyte Entry to Lymph Nodes. *Cell reports* **26**, 3116-3131.e3115 (2019).

55. Phng, L.K. & Gerhardt, H. Angiogenesis: a team effort coordinated by notch. *Developmental cell* **16**, 196-208 (2009).

56. Vanlandewijck, M.*, et al.* A molecular atlas of cell types and zonation in the brain vasculature. *Nature* **554**, 475-480 (2018).

57. Cheng, H.W.*, et al.* Origin and differentiation trajectories of fibroblastic reticular cells in the

splenic white pulp. *Nature communications* **10**, 1739 (2019).

58. Naba, A.*, et al.* The matrisome: in silico definition and in vivo characterization by proteomics of normal and tumor extracellular matrices. *Molecular & cellular proteomics : MCP* **11**, M111.014647 (2012).

59. Severino, P.*, et al.* Human Lymph Node-Derived Fibroblastic and Double-Negative Reticular Cells Alter Their Chemokines and Cytokines Expression Profile Following Inflammatory Stimuli. *Frontiers in immunology* **8**, 141 (2017).

60. Phillips, R. & Ager, A. Activation of pertussis toxin-sensitive CXCL12 (SDF-1) receptors mediates transendothelial migration of T lymphocytes across lymph node high endothelial cells. *European journal of immunology* **32**, 837-847 (2002).

61. Xu, Q., Schett, G., Li, C., Hu, Y. & Wick, G. Mechanical stress-induced heat shock protein 70 expression in vascular smooth muscle cells is regulated by Rac and Ras small G proteins but not mitogen-activated protein kinases. *Circulation research* **86**, 1122-1128 (2000).

62. Ley, K. The role of selectins in inflammation and disease. *Trends in molecular medicine* **9**, 263-268 (2003).

63. Silva, M., Videira, P.A. & Sackstein, R. E-Selectin Ligands in the Human Mononuclear Phagocyte System: Implications for Infection, Inflammation, and Immunotherapy. *Frontiers in immunology* **8**, 1878 (2017).

64. Farr, L., Ghosh, S. & Moonah, S. Role of MIF Cytokine/CD74 Receptor Pathway in Protecting Against Injury and Promoting Repair. *Frontiers in immunology* **11**, 1273 (2020).

65. Cao, Z.*, et al.* Angiocrine factors deployed by tumor vascular niche induce B cell lymphoma invasiveness and chemoresistance. *Cancer cell* **25**, 350-365 (2014).

66. Wallach-Dayan, S.B.*, et al.* CD44-dependent lymphoma cell dissemination: a cell surface CD44 variant, rather than standard CD44, supports in vitro lymphoma cell rolling on hyaluronic acid substrate and its in vivo accumulation in the peripheral lymph nodes. *Journal of cell science* **114**, 3463-3477 (2001).

67. Higashi, M.*, et al.* CD44 expression during tumor progression of follicular lymphoma. *Oncology reports* **22**, 1135-1140 (2009).

68. Drillenburg, P. & Pals, S.T. Cell adhesion receptors in lymphoma dissemination. *Blood* **95**, 1900-1910 (2000).

69. Ashkenazi, A. Targeting death and decoy receptors of the tumour-necrosis factor superfamily. *Nature reviews. Cancer* **2**, 420-430 (2002).

70. Pandey, S.*, et al.* IL-4/CXCL12 loop is a key regulator of lymphoid stroma function in follicular lymphoma. *Blood* **129**, 2507-2518 (2017).

71. Novak, A.J.*, et al.* Genetic variation in B-cell-activating factor is associated with an increased risk of developing B-cell non-Hodgkin lymphoma. *Cancer research* **69**, 4217-4224 (2009).

72. Gerli, M.F.M., *et al.* Combined Notch and PDGF Signaling Enhances Migration and Expression of Stem Cell Markers while Inducing Perivascular Cell Features in Muscle Satellite Cells. *Stem cell reports* **12**, 461-473 (2019).

73. Rehm, A., *et al.* Cooperative function of CCR7 and lymphotoxin in the formation of a lymphoma-permissive niche within murine secondary lymphoid organs. *Blood* **118**, 1020-1033 (2011).

74. Jacobs, J., *et al.* CD70: An emerging target in cancer immunotherapy. *Pharmacology & therapeutics* **155**, 1-10 (2015).

75. Starzer, A.M. & Berghoff, A.S. New emerging targets in cancer immunotherapy: CD27 (TNFRSF7). *ESMO open* **4**, e000629 (2020).

76. Yang, Z.Z., *et al.* TGF-β upregulates CD70 expression and induces exhaustion of effector memory T cells in B-cell non-Hodgkin's lymphoma. *Leukemia* **28**, 1872-1884 (2014).

77. Al Sayed, M.F., *et al.* CD70 reverse signaling enhances NK cell function and immunosurveillance in CD27-expressing B-cell malignancies. *Blood* **130**, 297-309 (2017).

78. Project, I.N.-H.s.L.P.F. A predictive model for aggressive non-Hodgkin's lymphoma. *The New England journal of medicine* **329**, 987-994 (1993).

79. Taskinen, M., *et al.* Prognostic impact of CD31-positive microvessel density in follicular lymphoma patients treated with immunochemotherapy. *European journal of cancer (Oxford,*

England : 1990) **46**, 2506-2512 (2010).

80. Nagakubo, D.*, et al.* A high endothelial venule secretory protein, mac25/angiomodulin, interacts with multiple high endothelial venule-associated molecules including chemokines. *Journal of immunology (Baltimore, Md. : 1950)* **171**, 553-561 (2003).

81. Janatpour, M.J., Hudak, S., Sathe, M., Sedgwick, J.D. & McEvoy, L.M. Tumor necrosis factor-dependent segmental control of MIG expression by high endothelial venules in inflamed lymph nodes regulates monocyte recruitment. *The Journal of experimental medicine* **194**, 1375-1384 (2001).

82. Miyasaka, M. & Tanaka, T. Lymphocyte trafficking across high endothelial venules: dogmas and enigmas. *Nature reviews. Immunology* **4**, 360-370 (2004).

83. González-González, L. & Alonso, J. Periostin: A Matricellular Protein With Multiple Functions in Cancer Development and Progression. *Frontiers in oncology* **8**, 225 (2018).

84. Noh, K.*, et al.* Differential Effects of EGFL6 on Tumor versus Wound Angiogenesis. *Cell reports* **21**, 2785-2795 (2017).

85. An, J.*, et al.* EGFL6 promotes breast cancer by simultaneously enhancing cancer cell metastasis and stimulating tumor angiogenesis. *Oncogene* **38**, 2123-2134 (2019).

86. Cremasco, V.*, et al.* FAP Delineates Heterogeneous and Functionally Divergent Stromal Cells in Immune-Excluded Breast Tumors. *Cancer immunology research* **6**, 1472-1485 (2018).

87. Costa, A., *et al.* Fibroblast Heterogeneity and Immunosuppressive Environment in Human Breast Cancer. *Cancer cell* **33**, 463-479.e410 (2018).

88. Kieffer, Y., *et al.* Single-Cell Analysis Reveals Fibroblast Clusters Linked to Immunotherapy Resistance in Cancer. *Cancer discovery* **10**, 1330-1351 (2020).

89. Baker, A.M., *et al.* Lysyl oxidase plays a critical role in endothelial cell stimulation to drive tumor angiogenesis. *Cancer research* **73**, 583-594 (2013).

90. Opitz, C.A., *et al.* The therapeutic potential of targeting tryptophan catabolism in cancer. *British journal of cancer* **122**, 30-44 (2020).

91. Jacobs, J., *et al.* Unveiling a CD70-positive subset of cancer-associated fibroblasts marked by pro-migratory activity and thriving regulatory T cell accumulation. *Oncoimmunology* **7**, e1440167 (2018).

92. Béguelin, W., *et al.* Mutant EZH2 Induces a Pre-malignant Lymphoma Niche by Reprogramming the Immune Response. *Cancer cell* **37**, 655-673.e611 (2020).